École polytechnique de Louvain

Including drone attitude in SKA calibration

Author: **Alexandre Pierlot**
Supervisor: **Christophe Craeye**
Readers: **Eloy De Lera Acedo, François Glineur, Claude Oestges**
Academic year 2022–2023
Master [120] in Electro-mechanical Engineering

We live in a very special time: the only time when ce can observationally verify than we live in a very special time

---

Lawrence Krauss

Université Catholique de Louvain

Abstract

Ecole Polytechnique de Louvain

Including UAV attitude in SKA calibration

by Alexandre Pierlot

The Square Kilometer Array will be one of the main astronomical instruments of the 21 century [1]. The Array will be composed of two types of telescopes, the SKA-Mid and SKA-Low. The SKA-Low will consist of multiple stations, each station will be composed of 256 SKALA (Square Kilometer Log-periodic Antenna) antennas [2].
In order to acquire high resolution images, a calibration of the arrays will need to be achieved. The Far-Field calibration of such array will require artificial signal sources such as antennas mounted on Unmanned Aerial Vehicle (UAV). Previous investigation has proven that Far-Field calibration error was mainly due to the UAV attitude errors [3].
This thesis focuses on the reduction of the calibration error by calculating the UAV attitudes using the SKALA elements composing the SKA stations. The HARP software is used in order to calculate the embedded element pattern (EEP) of each antenna. The calculation of the voltage received by the illumination of the array using the UAV is detailed and verified. We develop a method to calculate the UAV attitudes allowing to improve the calculation of the calibration coefficients of the array. The Levenberg-Marquardt and Nelder-Mead algorithms are used and a performance comparison is carried out for each algorithm. The impact of the thermal noise of the low noise amplifier (LNA) and the sky is modelled in the received voltage. The impact of this thermal noise on the accuracy of the calibration calculation, using the developed algorithm, focused on.

Acknowledgments

First I would like to thank my advisor, Prof. Christophe Craeye for his support, advice and guidance throughout this Master thesis.

I would also like to thank Dr. Jean Cavillot, for all his explanations and technical support about HARP.

I would like to express my gratitude to Prof. Eloy de Lera Acedo for his advice about the SKALA array models.

Next I would like to thank Prof. François Glineur, for his advice about the resolution of the different mathematical problems.

Furthermore, I would like to thank the team of the Kot Astro, who rekindled my passion for astronomy and led me to choose this subject.

Finally, I would like to express my gratitude to my parents, for their support to date.

Contents

List of Figures

List of Tables

Abbreviations

AUT **A**ntenna **U**nder **T**est

AAVS **A**perture **A**rray **V**erification **S**ystem

EEP **E**mbedded **E**lement **P**attern

HARP **HAR**monic **P**olynomial

L-M **L**evenberg-**M**arquardt

LNA **L**ow **N**oise **A**mplifier

MBF **M**acro **B**asis **F**unction

MoM **M**ethod **o**f **M**oments

N-M **N**elder-**M**ead

N-R **N**ewton-**R**aphson

UAV **U**nmanned **A**erial **V**ehicle

SNR **S**ignal to **N**oise **R**atio

SKA **S**quare **K**ilometer **A**rray

SKALA **S**quare **K**ilometer **A**rray **L**og-periodic **A**ntenna

Nomenclature

λ	Wavelength
$\mathbf{F}_k^d$	Embedded element pattern of dipole k
$\mathbf{F}_{cal}^i$	Calibrated EEP of antenna i
$\mathbf{P}_{p,i_a}^i$	Pondered sum of the radiation pattern of MBFs on antenna i_a acting on antenna i and pointing towards position p
$\mu_{\varepsilon,\phi}$	mean error of ϕ
θ	zenith angle
$\tilde{V}_p^i$	Simulated measurement of the voltage at antenna i illuminated by the UAV at position p
ε_ϕ	ϕ error
φ	azimuth angle
$c_{i_a}^i$	Calibration coefficient associated to i_a antenna interacting with antenna i
cf_{i_m,i_a}^i	MBF coefficient computed using HARP
D	Array diameter [m]
k	Wavenumber
N_a	Number of antennas
N_p	Number of drone positions
p_{h,i_m}	horizontal component of the radiation pattern of MBF i_m
p_{v,i_m}	vertical component of the radiation pattern of MBF i_m
$V_{i_a,k}^r$	Simulated voltage received by antenna i_a
Z_L	Load impedance of the SKALA antennas

Chapter 1

Introduction

Radio astronomy instruments evolved from simple structures composed of 2 antenna interferometers to complex arrays composed of dozens of steerable elements [8]. The increase in the size of telescopes, combined with ever more advanced technology, has enabled astronomers to observe objects never before seen, pushing back the limits of the observations even further. Recent years have seen the emergence of even more sophisticated telescopes. One can note the James Webb Space Telescope, that recently observed infrared galaxies 600 million years after the Big Bang [9] or the Event Horizon Telescope, fruit of collaboration between several radio telescopes around the globe, that provided the first image of a black hole in 2019 [10].

The extremely large arrays concept for radio astronomy was developed during the 90's. Those arrays would have allowed to reach even higher resolution imaging, with a collecting area two orders of magnitude greater than before. Those radiotelescopes would be composed of multiple arrays, with a baseline approaching 5000 Km [11].

The Square Kilometer Array The Square Kilometer Array (SKA) development began in 1993 and will herald a turning point in the domain of radio astronomy. The SKA is the result of an international project with the aim to probe a wide range of elements. The SKA will make it possible to study the Cosmic Dawn and the Epoch of Reionisation, the nature of Dark Energy and the evolution of galaxies [1]. This radio telescope will be composed of two different telescopes, SKA1-Mid and SKA1-Low as shown in Fig. 1.1, with different structures and antennas used. While the SKA1-Mid will operate between 350 MHz and 15.4 GHz, the SKA1-Low will be charged to detect signals from 50 MHz to 350 MHz [2].

(a) SKA1-MID array

(b) SKA1-LOW multiple arrays

Figure 1.1: Artist impressions of SKA telescopes, from [4, 5].

The SKA-Low telescope will be composed of 512 stations placed in a central core and along 3 spiral arms in Australia. As each station will be composed of 256 Square Kilometer Array Log-Periodic Antennas (SKALA), the SKA-Low telescope will be composed of 131072 log-periodic, dual polarized antennas [2, 1]. Several versions of the antennas were developed over the course of the project, resulting in version 4.1 of the antenna, as shown in Fig. 1.2 [2].

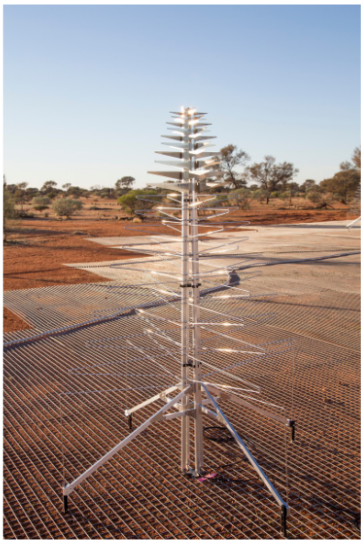

Figure 1.2: Single SKALA4.1 antenna composing the SKA-Low telescope, from [2].

Several station prototypes, known as Aperture Array Verification System (AAVS), have already been built serving as a test platform for the technologies and methods developed for the design of the SKA-Low [2, 12, 13]. The AAVS0 was composed of 16 random sparse distributed SKALA1 antennas [12] while the AAVS1 comprises 256 SKALA2 antennas [13].

Calibration The instrumental and atmospheric factors generate distortions in the received signals. The aim of the calibration is to remove those effects in order to synthesise high-resolution images [8]. During the calibration procedure, the instrumental factors such as antennas positions and axis misalignment, are supposed to be stable over time [11]. As the SKA stations are large, using an anechoic chamber is impossible for those arrays. One method proposed is to use an Unmanned Aerial Vehicle (UAV) and calibrate the arrays, as explained in [14]. However, the UAV attitudes and positions are generally biased during an UAV flyover [15], leading to generate errors in the calibration coefficients of the arrays [3]. This text focuses on a method to estimate the UAV attitudes and then increase the precision of the calibrations.

Structure of the thesis This work is organized as follows: first, the state-of-the-art is presented, focusing on the Embedded Element Pattern computation and calibration of the array. The Harmonic Polynomial (HARP) software used to calculate the Embedded Element Pattern (EEP) is described.
Chapter 3 focuses on the implementation of the SKALA and UAV coupling, where the SKALA array and UAV properties will be described. The calculation of the received voltage on the SKALA antennas is explained and verified within simulations.
The next chapter is devoted to the calculation of the attitude of the UAV with a calibrated SKALA array to prove such methods as possible. The algorithms used to calculate the attitudes of the UAV are described. Then, a comparison of the effectiveness of the presented algorithms is carried on. It allows to choose the most suitable algorithms for the next chapters.
Chapter 5 focuses on the implementation of the rectification of the coefficients, using the deduction of the UAV attitudes based on the measured voltages of the array. The calibration errors with and without rectification are compared to confirm the choice of the method used in the Chapter 6.
Finally, Chapter 6 describes the application of the chosen algorithm while including noised signals. As the amplifiers and the sky indeed leads to interference in the measured voltage, the modeling of those elements is described. Then the impact of the thermal noise on the effectiveness of the proposed method is evaluated.

Chapter 2

State of the art

In this chapter the state-of-the-art of the numerical simulation and calibration of the SKA stations will be developed.

The method used in HARP for calculation the Embedded Element Pattern (EEP) of each SKALA antennas will be described. The principles of calibration for large arrays will then be focused on, investigating on the calibration using artificial sources in far field.

2.1 EEP computation of SKALA antenna using HARP

Since the data of the measurements were not available, using simulations in order to compute the EEP of each SKALA antennas was mandatory. Therefore, the HARP software, standing for HARmonic Polynomial, was used to achieve those simulations. This software allows fast simulations of the EEP of the SKALA antennas using Macro Basis Functions (MBF) as explainted in [6]. The method used by HARP allows to accelerate the calculation of the interactions between antennas. It has been tested on SKALA arrays, allowing to simulate fields measurements and compute the impact of the error of the UAV positions on the EEP reconstitution [14].

2.1.1 Method of Moments

Computing the radiation pattern of a SKALA antenna requires to deduce its radiated electric field by solving Maxwells equations. However, these equations need to be integrated on complex structures, which might not be solved analytically. A solution can still be approached using computational methods such as the method of moments (MoM), transforming the integral equations into a linear problem [7].

The Methods of Moments is fully explained in [7] and then won't be detailed in this text. Still, summarizing the main principles is important to understand the purpose of HARP.

As shown in Fig. 2.1, SKALA2 antennas have a complex geometry, integration the Maxwell equations on the antenna is then not possible analytically. By decomposing the domain of integration into N subdomains, as shown in Fig. 2.2, it is possible to divide the problem into multiple simpler problems and linearize the integral equations.

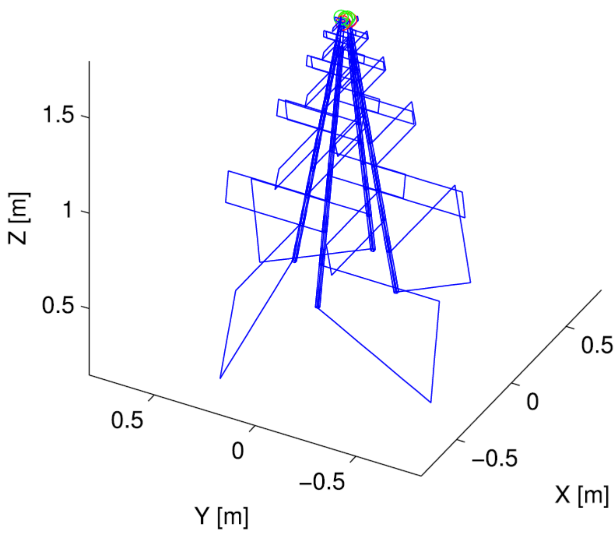

Figure 2.1: SKALA2 mesh, from [6]

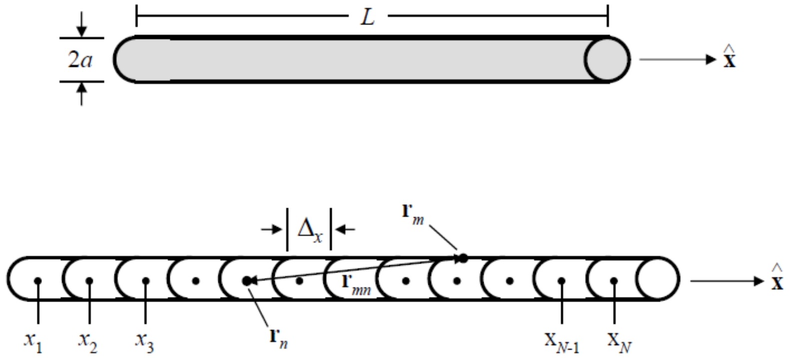

Figure 2.2: Division of a wire into N subdomains, from [7]

By supposing the integral of the complex domain as a sum of *basis functions* f_n on all the subdomains multiplied by a respective weight a_n, it is possible to linearize the problem as

$$f \approx \sum_{n=1}^{N} a_n f_n \tag{2.1}$$

where f is the unknown function. An example of the method is shown at Fig. 2.3

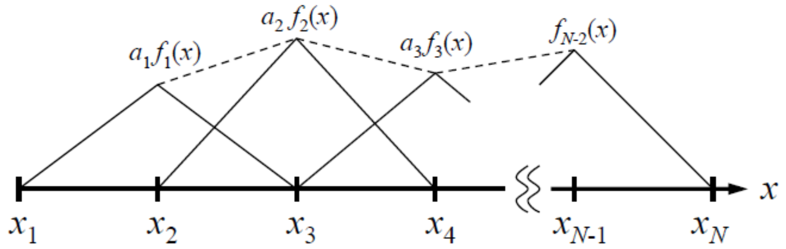

Figure 2.3: Linearization of the problem by using simpler integrals f_n multiplied by a weight a_n, from [7]

Applying a linear operator $\mathcal{L}$ to the basis functions f_n and using an inner product or *moment* $<,>$ (such as multiplication of the integrals) with a testing function f_m lead to rewrite the equation as

$$< f_m, g > \approx \sum_{n=1}^{N} a_n < f_m, \mathcal{L}(f_n) > \quad \forall m = 1, \ldots, M \tag{2.2}$$

where $g = \mathcal{L}(f)$.
Calculating the value using N testing functions f_m results in a $N \times N$ equation system

$$\mathbf{Za} = \mathbf{b} \tag{2.3}$$

where $z_{m,n} =< f_m, \mathcal{L}(f_n) >$ is called the *impedance matrix* in our case, $\mathbf{a}$ the vector containing the weights a_n and $b_m =< f_m, g >$.

Solving such equation systems can be done using Gaussian elimination. However, the solution complexity of the MoM is $\mathcal{O}((N_a N_b)^3)$ where N_a is the number of antennas and N_b the number of basis functions [6]. Computing the EEP of each SKALA antenna requires to calculate the impedance matrix multiple times, leading to high computation time on large arrays.

2.1.2 Macro Basis Functions used in HARP

In order to reduce the computation time in the MoM, a compression of the impedance matrix is done by replacing the basis functions by a new set of macro basis functions (MBF). Those MBFs are obtained by solving smaller problems [6]. This method allows to calculate the solution directly by avoiding iteration for multiple antennas [16, 17].

By replacing the set of basis functions by a set of MBF, the complexity of the system of equations is then reduced to $\mathcal{O}((N_a N_m)^3)$, where N_m is the number of MBF. If $N_m \ll N_b$, the MBF method highly accelerates the calculations [6]. Calculating all the EEPs of 200 antennas composing an array can be done in 2 hours [18].

Even if the computation time of the EEP is highly reduced, the impedance matrix filling complexity is still $\mathcal{O}((N_a N_b)^2)$, becoming dominant in the computation time while using fine mesh. The interactions between the MBF on two similar antennas can still be interpolated using harmonic polynomial (HARP) expressions [17]. This technique allows to compute the MBF interactions independently from the number of antennas, still accelerating the calculation of the EEP.

The HARP method used was previously tested on SKALA arrays, allowing to calculate the EEP of the antennas composing an irregular array with accuracy as well as the mutual coupling of the antennas [17, 18, 19].

2.2 Array calibration using UAV

The calibration of radio telescopes is a critical step in order to acquire correct measurements. This calibration has to take into account the phase and gain of the antennas and the atmospheric disturbances [8].

Pattern calculation The calculation of the radiation pattern of the whole array is equal to the sum of each EEP of the antennas. Due to coupling between antennas, each element composing the array influences every EEP [3]. This impact of each antenna is calculated via the MBF interactions. In other words, the N_m MBF of one antenna influences the EEP of each other antenna surrounding it. HARP then computes the EEP, centered to the origin, of the antenna i using the following equation [6]

$$\mathbf{F}^i(\theta, \varphi) = \sum_{i_m=1}^{N_m} \sum_{i_a=1}^{N_a} cf^i_{i_m, i_a} \mathbf{p}_{i_m}(\theta, \varphi) e^{jk(x_{i_a} u_x + y_{i_a} u_y)} \tag{2.4}$$

where $cf^i_{i_m, i_a}$ is the coefficient for the MBF i_m on antenna i_a when only antenna i is ON, $\mathbf{p}_{i_m} = p_{v,i_m} \hat{\mathbf{e}}_\theta + p_{h,i_m} \hat{\mathbf{e}}_\varphi$ is the polarization vector (vertical and horizontal) of the MBF i_m, (x_{i_a}, y_{i_a}) is the position of the antenna i_a and (u_x, u_y, u_z) is a unit vector in the direction of interest (θ, φ).

Finally, the array pattern is calculated by summing each EEP multiplied by a respective beamforming weight w_i

$$\mathbf{F}_{array}(\theta, \varphi) = \sum_{i=1}^{N_a} w_i \mathbf{F}^i(\theta, \varphi) \tag{2.5}$$

Calibration coefficients To compute the EEP of each antenna, each EEP requires to be calibrated by multiplying the MBF interactions by a coefficient $c^i_{i_a, i_m} \in \mathbb{C}$. The equation of the calibrated EEP of antenna i then becomes [14]

$$\mathbf{F}^i_{cal}(\theta, \varphi) = \sum_{i_m=1}^{N_m} \sum_{i_a=1}^{N_a} cf^i_{i_m, i_a} \mathbf{p}_{i_m}(\theta, \varphi) e^{jk(x_{i_a} u_x + y_{i_a} u_y)} c^i_{i_a, i_m} \tag{2.6}$$

Supposing N_a antennas, the N_a EEPs are calculated using N_m MBF per antenna, the number of calibration coefficients for the array is then $N_a^2 N_m$. If each antenna is modeled using 20 MBF, a 256 antennas array then requires $256^2 20 = 1310720$ calibration coefficients. Solving this number of unknown requires at least as much experiments, involving excessive amount of resources, for both measurements and calculation. To reduce the complexity of the calibration problem, one alternative is to suppose one coefficient per antenna $c^i_{i_a}$ [14], leading to reduce the number of unknowns to $N_a N_m = 5120$, which is a much more affordable number of coefficients. The calibrated EEP of the antenna i then becomes

$$\mathbf{F}^i_{cal}(\theta, \varphi) = \sum_{i_m=1}^{N_m} \sum_{i_a=1}^{N_a} cf^i_{i_m,i_a} \mathbf{p}_{i_m}(\theta, \varphi) e^{jk(x_{i_a} u_x + y_{i_a} u_y)} c^i_{i_a} \tag{2.7}$$

This equation can be written in matrix form by taking each component of the polarization $\mathbf{p}_{i_m}$ one by one, as example for the vertical component of the radiation pattern of MBF i_m, p_{v,i_m} [3]

$$\mathbf{F}^i_{v,cal}(\theta, \varphi) = \sum_{i_a=1}^{N_a} \sum_{i_m=1}^{N_m} cf^i_{i_m,i_a} p_{v,i_m}(\theta, \varphi) e^{jk(x_{i_a} u_x + y_{i_a} u_y)} c^i_{i_a} = \mathbf{B}^i_v \mathbf{c}^i \tag{2.8}$$

where $\mathbf{B}^i_v \in \mathbb{C}^{N_m \times N_a}$.

Because of the size of the AAVS0 and AAVS1, a method to deduce the EEP of each antenna using Unmanned Aerial Vehicles (UAV) was developed to measure the array properties. The illumination of the array can be done using mounted antennas on the drone, leading to deduce the calibration coefficients for each antenna, as explained in [3]. This method will be developed in the next chapter.

Chapter 3

SKALA array and UAV coupling

This chapter focuses on the implementation of the SKALA array coupling with a dipole placed on a UAV.
We will first explain the modeling of the SKALA arrays and the choice of each array modelled. Then we will focus on the UAV modelling, such as its antennas and its path. The method to compute the voltage from antennas interactions will then be explained as well as the computation of the calibration coefficients. Finally, an analysis of the attitude and position error of the drone on the voltage will be investigated, the error of voltage for different configurations will be analysed, including the calibration error using different number of positions.

3.1 SKALA array modelling

Since working directly on a 256 antennas array might have been time and resource-consuming, testing the simulations with a reduced number of antennas were useful in order to verify the correct implementation of the code. Four arrays, containing different number of SKALA antennas, were used.
The first array was composed of only one antenna, mainly used to develop and rapidly validate the simulations. The second one was composed of four antennas, it was used to rapidly verify simulations for arrays composed of multiple antennas. The third configuration was composed of 16 antennas, similarly to the AASV0 array [12], used to validate simulations on a more complex array configuration.
The last array considered corresponds to a SKA1-Low station, composed of 256 associated SKALA2 antennas. The configuration of each arrays is shown in Fig. 3.1.

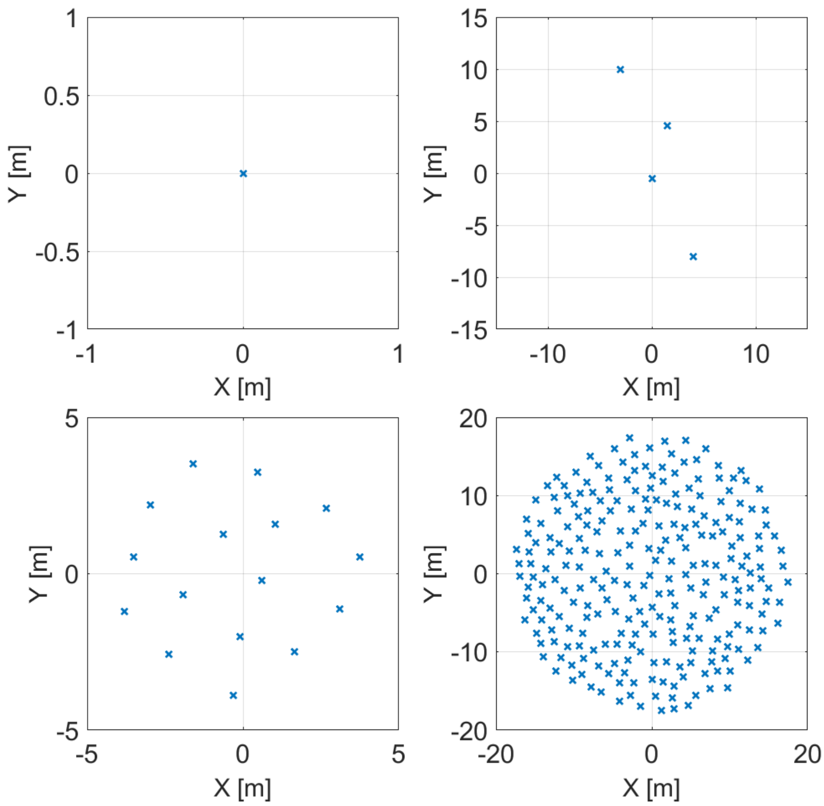

Figure 3.1: Positions of the SKALA antennas for each simulated array

3.2 UAV modelling

3.2.1 Frame and rotation axis

The UAV was modelled a as single point carrying two ideal, zero length, dipole antennas oriented along the X and Y axis of the drone frame. Those dipoles were supposed to be placed at the center of the UAV frame.

Instead of using Trait-Bryan angles α, β, γ corresponding to Z-Y-X *intrinsic* rotations as explained in [3], a choice of α, β, γ corresponding to Z-X-Y intrinsic rotations was implemented. This choice was arbitrary and seemed easier to manipulate. The initial orientation of the UAV frame was furthermore changed, with a Z axis pointing towards the sky when the drone was not tilted. The illustration of those two frames is shown in Fig. 3.2.

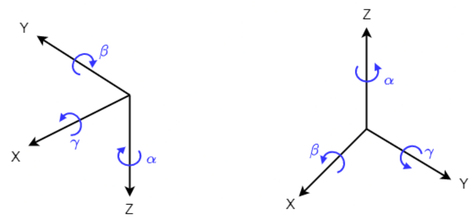

Figure 3.2: Rotation angles on UAV frame, left : Trait-Bryan, right : angles used

3.2.2 UAV path model

In order to perform a far field calibration, the UAV must be at a minimum distance given by the Faunhoffer condition [20]

$$r \gg \frac{2D^2}{\lambda} \tag{3.1}$$

with D the diameter of the array, λ the wavelength of the signal.

Since the SKA1-Low will operate between 50 MHz and 350 MHz [12], in order to meet the far-field criteria, the UAV must fly at a distance of about 3 km from the array, which was considered to be unattainable in such conditions. A more realistic approach was to consider a far-field overflight for the antennas, while remaining in the near field for the array. The height of a SKALA antenna being approximately 1.8 m [21], the far field condition gave a distance of about 7.5 m.

Ideal drone trajectory The entire drone flyby was assumed to be at a height of 100 m to ensure the far field criteria. The drone performed a series of circular trajectories centred on the middle of the array. Experiments were performed at regular intervals during the circular path. It was thus possible to vary the number of simulations by increasing the number of circles or to increase the number of samples per circle performed. An illustration of the trajectory is shown at Fig. 3.3.

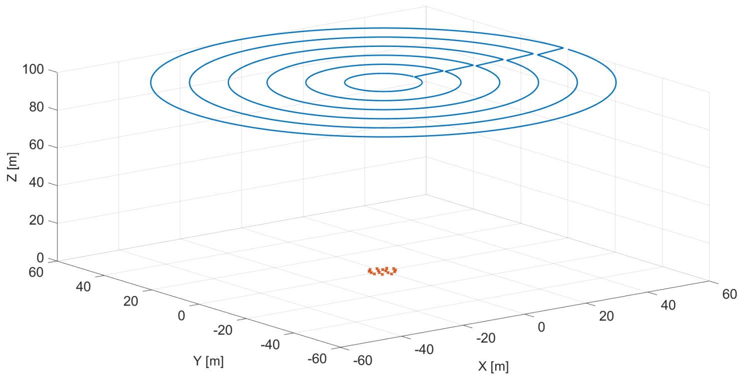

Figure 3.3: Typical trajectory of the UAV flying over the 16 SKALAs array

Error model of the drone trajectory As the calibration will take place in an outdoor environment, it is necessary to take into account the position and orientation errors of the UAV along the trajectory. The error in the measurement of the position of a UAV in the context of antenna performance measurements has already been studied, typical error values from [15, 22] were used and are listed in Table 3.1.

Since the orientation error of the UAV also affects the quality of the measurements, it has been taken into account. The estimation of the average error of the measured orientation [15], including the controlled orientation error, has also been investigated [23]. In this case, only the measurement error was taken into account, it is also listed in Table 3.1.

Impacted element	X [m]	Y [m]	Z [m]	α [°]	β [°]	γ [°]
Standard deviation error	0.02	0.02	0.05	1.93	0.141	0.156

Table 3.1: Error parameters on the drone position and attitude

The error was finally modelled, for each parameter taken individually, as a Gaussian distribution with a mean equal to the objective position or orientation, adding this distribution allowed us to generate noisy positions and attitudes.

3.3 Voltage computation for Drone-SKALA interaction

3.3.1 Voltage computation

The computation of the received voltage was done individually for each antenna in the array and for each position $p \in \{1, 2, ..., N_p\}$ of the UAV. Assuming an antenna $k \in \{1, 2\}$, placed on the UAV, individually excited by a voltage source V_k^t, the voltage $V_{i,k,p}$ received by the SKALA antenna i can be obtained by the following equation [3]:

$$V_{k,p}^i = \frac{2\lambda Z_L}{j\eta} \mathbf{F}_k^d \cdot \mathbf{F}^i \frac{e^{-jkR_{i,p}}}{R_{i,p}} V_k^t \tag{3.2}$$

where $\mathbf{F}_k^d$ stands for the radiation pattern of the UAV mounted dipole k, $\mathbf{F}^i$ corresponds to the radiation pattern of the SKALA antenna i, $R_{i,p}$ stands for the distance between the SKALA antenna i and the drone position p, Z_L stands for the load impedance terminating the SKALA antenna.

From equation (3.2) and (2.7), the voltage equation can be written as

$$V_p^i = \frac{2\lambda Z_L}{j\eta} V_k^t \sum_{i_a=1}^{N_a} c_{i_a}^i \mathbf{F}_k^d(\hat{u}_{ia}, \Omega) \cdot \sum_{i_m=1}^{N_m} cf_{i_m,i_a}^i \mathbf{p}_{i_m}(\theta, \varphi) e^{jk(x_{i_a} u_x + y_{i_a} u_y)} \frac{e^{-jkR_{i_a,p}}}{R_{i_a,p}} \tag{3.3}$$

The pondered N_m sum of the MBFs on antenna i_a can be seen as a "macro" MBF contributing to the EEP of antenna i. Applying the equation (3.2) on each macro MBF can be seen as the contribution of each macro MBF i_a to the voltage on antenna i. Futhermore, calculating those voltages contribution using this method doesn't require to apply a phase shift on each macro MBF to center the phase at the origin, since the direct interaction between the UAV and the macro MBF is computed.

It is possible to use the following notation to write the equation (3.3) in compact form :

$$\mathbf{P}_{p,i_a}^i = \frac{2\lambda Z_L}{j\eta} V_k^t \sum_{i_m=1}^{N_m} cf_{i_m,i_a}^i \mathbf{p}_{i_m}(\theta, \varphi) \frac{e^{-jkR_{i_a,p}}}{R_{i_a,p}} \tag{3.4}$$

All the elements used in eq (3.3) and (3.4) are supposed to be known except the calibration coefficients, deducing the coefficients $c_{i_a}^i$ is equivalent to solve the system of equations

$$\sum_{i_a=1}^{N_a} \mathbf{F}_k^d(\hat{u}_{i_a,p}, \Omega) \cdot \mathbf{P}_{i_a}^i c_{i_a}^i = \tilde{V}_p^i \quad \forall p \tag{3.5}$$

where $\tilde{V}_p^i$ is the measured voltage of antenna i with the UAV a position p.

Since the calibration is carried on using p drone positions, equation 3.5 can be written in matrix form :

$$\begin{bmatrix} \mathbf{F}^d_{1,1} & \dots & \mathbf{F}^d_{1,N_p} \\ & \vdots & \\ \mathbf{F}^d_{N_a,1} & \dots & \mathbf{F}^d_{N_a,N_p} \end{bmatrix} \begin{bmatrix} \mathbf{P}^i_{1,1} & \dots & \mathbf{P}^i_{1,N_a} \\ & \vdots & \\ \mathbf{P}^i_{N_p,1} & \dots & \mathbf{P}^i_{N_p,N_a} \end{bmatrix} \mathbf{c}^i = \tilde{\mathbf{V}}^i \tag{3.6}$$

where $\mathbf{F}^i_{i_a,p}$ is the value of the radiation pattern of the UAV dipole at position p pointing towards the antenna i_a, $\mathbf{P}^i_{p,i_a}$ the radiation pattern of the macro MBF of antenna i_a pointing towards the UAV at position p, multiplied by a constant as defined in eq (3.4). $\tilde{\mathbf{V}}^i \in \mathbb{C}^{N_p}$ stands for the column vector containing the voltages from the illumination of the SKALA antenna by the UAV at the N_p positions.

Resources and calculation cost The radiation pattern of each macro MBF requires to be stored to calculate the voltage on each antenna. The radiation pattern of each N_m MBF, calculated by HARP, is stored as a $\mathbb{C}^{91\times361}$ matrix. The radiation pattern of each macro MBF, used to calculate the N_a EEPs, is then stored as a $\mathbb{C}^{91\times361\times N_a\times N_a\times2}$ matrix, where the "2" factor comes from the consideration of the vertical and horizontal polarizations of the radiation patterns. This variable then requires a high amount of space in the memory, especially when using 256 antennas, leading to store $256^2 \times 91 \times 361 \times 2 = 4305846272$ *complex values* and then could not be used on a computer using 32 GB RAM. Since each antenna EEP is defined by a $\mathbb{C}^{91\times361\times256\times2}$ matrix, and the computation of the calibration coefficient is independent from each antenna, it is still possible to decouple the problem and calculate the coefficients of each EEP independently.
Furthermore, simulating the received voltage of each antenna using eq. (3.6) leads to a matrix filling minimum complexity of $\mathcal{O}(N_a^3)$ to solve N_a^2 coefficients. The matrix filling is then the dominant element in the calibration calculation time.

The computation time for the array composed of the 256 antennas could still be estimated from the simulations of the 4 antenna array. Simulations on a computer using a processor Intel i7-12700 was used with a flyover of 16 positions. The simulation lasted approximately 0.336 seconds for the 4 SKALA antennas. The calculation time of the coefficients for 256 antennas was then estimated to $0.336 \times (256/4)^3 \approx 88 \times 10^3$ seconds, which corresponds to an entire day of simulations using a similar computer. For those explained reasons, this text is mainly based on an array composed of 4 SKALA antennas.

Computation of the scalar product Since the antenna and dipole EEPs of the UAV are expressed in their own spherical basis, it is necessary to perform basis transformations in order to perform the scalar product. The radiation pattern of the macro MBF, associated to their respective SKALA antennas, and the UAV dipoles are initially given in a spherical base as shown in Fig. 3.4 [3].

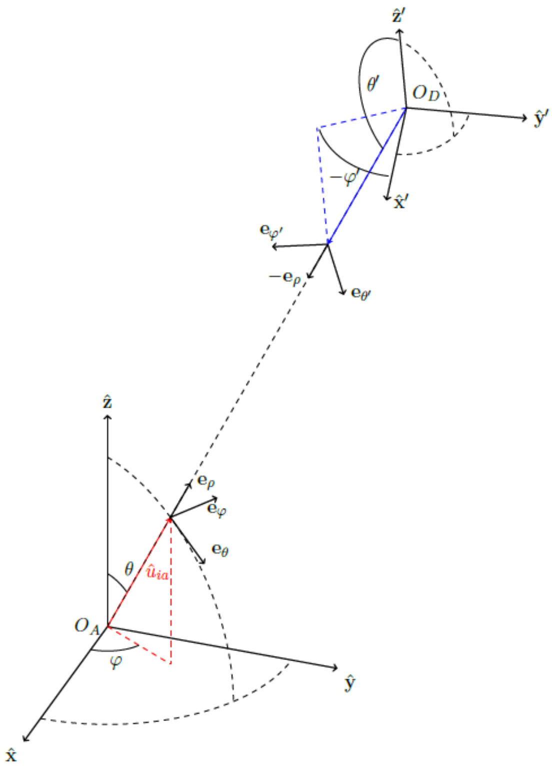

Figure 3.4: Sketch of the geometry, from [3]

Since the $\{\mathbf{e}_\rho, \mathbf{e}_\theta, \mathbf{e}_\varphi\}$ base of the SKALA antenna is expressed in spherical coordinates, the radiation pattern can be re-expressed in Cartesian coordinates using the following equation [3]

$$\begin{pmatrix} \mathbf{e}_\rho \\ \mathbf{e}_\theta \\ \mathbf{e}_\varphi \end{pmatrix} = \begin{pmatrix} \sin\theta\cos\varphi & \sin\theta\cos\varphi & \cos\theta \\ \cos\theta\cos\varphi & \cos\theta\sin\varphi & -\sin\theta \\ -\sin\varphi & \cos\varphi & 0 \end{pmatrix} \begin{pmatrix} \hat{\mathbf{x}} \\ \hat{\mathbf{y}} \\ \hat{\mathbf{z}} \end{pmatrix} = U(\rho', \theta', \varphi') \begin{pmatrix} \hat{\mathbf{x}} \\ \hat{\mathbf{y}} \\ \hat{\mathbf{z}} \end{pmatrix} \tag{3.7}$$

The process is similar for the drone base $\{\mathbf{e}'_\rho, \mathbf{e}'_\theta, \mathbf{e}'_\varphi\}$ with the coordinates $\{\rho', \theta', \varphi'\}$ to change to the cartesian base $\{\hat{\mathbf{x}}', \hat{\mathbf{y}}', \hat{\mathbf{z}}'\}$ of the drone.

To express the respective Cartesian coordinates of the drone and the SKALA antenna in the same frame, the rotations of the UAV have to be taken into account. By using the rotation matrices associated to the rotation angles, shown at Fig. 3.2, it is possible to express $\{\hat{\mathbf{x}}', \hat{\mathbf{y}}', \hat{\mathbf{z}}'\}$ into $\{\hat{\mathbf{x}}, \hat{\mathbf{y}}, \hat{\mathbf{z}}\}$ and vice versa using

$$\begin{pmatrix} \hat{\mathbf{x}} \\ \hat{\mathbf{y}} \\ \hat{\mathbf{z}} \end{pmatrix} = A_z(\alpha)A_x(\beta)A_y(\gamma) \begin{pmatrix} \hat{\mathbf{x}}' \\ \hat{\mathbf{y}}' \\ \hat{\mathbf{z}}' \end{pmatrix} = T(\alpha, \beta, \gamma) \begin{pmatrix} \hat{\mathbf{x}}' \\ \hat{\mathbf{y}}' \\ \hat{\mathbf{z}}' \end{pmatrix} \tag{3.8}$$

where A_z, A_y, A_x are the rotation matrices defining the intrinsic rotations around the (Z, Y, X) axis respectively.

It is finally possible to compute the voltage from the scalar product using the EEP of the SKALA antenna and the drone dipole [3]:

$$\mathbf{F}^d_{k,i_a,p} \cdot \mathbf{P}^i_{p,i_a} = \begin{pmatrix} F^d_{k,i_a,p,\theta'} & F^d_{k,i_a,p,\varphi'} \end{pmatrix} \left[U(\theta',\varphi') T^T(\alpha,\beta,\gamma) U^T(\theta',\varphi') \right]^T \begin{pmatrix} P^i_{\theta,p,i_a} \\ P^i_{\varphi,p,i_a} \end{pmatrix} \tag{3.9}$$

However, since HARP calculates the radiation pattern of each MBF based on discrete spherical orientations, an interpolation of the vertical and horizontal polarization of those radiation patterns needs to be carried out. The interpolation method was computed using 2D linear interpolation for both polarizations.

3.3.2 Voltage computation results

As a first step, a voltage calculation was performed using a single antenna to verify the correct implementation of the method.

We assumed here that the UAV trajectory is not biased, both in terms of positions and orientation. The UAV followed a trajectory while keeping its reference frame parallel to that of the antenna array.

Initially, only one antenna was considered to verify the validity of the code. The simulation of the flyover was carried out with 4 different configurations. Those configurations are shown at Table 3.2.

Parameter	Dipole orientation	SKALA polarization	frequency
Experiment 1	X	X	140MHz
Experiment 2	Y	Y	140 MHz
Experiment 3	Y	X	140MHz
Experiment 4	Y	X	110MHz

Table 3.2: Configuration for the different experiments simulated

Although the simulations did not take into account the phenomenon of antenna saturation, the dipole excitation value has been adjusted to simulate voltage values closer to reality. The excitation values for each experiment were therefore all assumed to be 5 mV. The results of the simulations can be seen in Fig. 3.5.

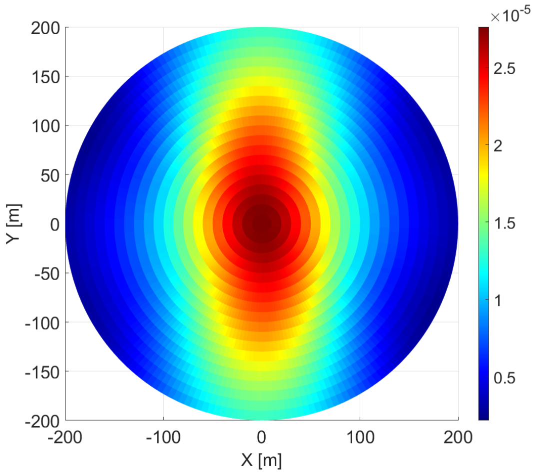

(a) Voltages with dipole on X axis, SKALA X polarization, experiment 1

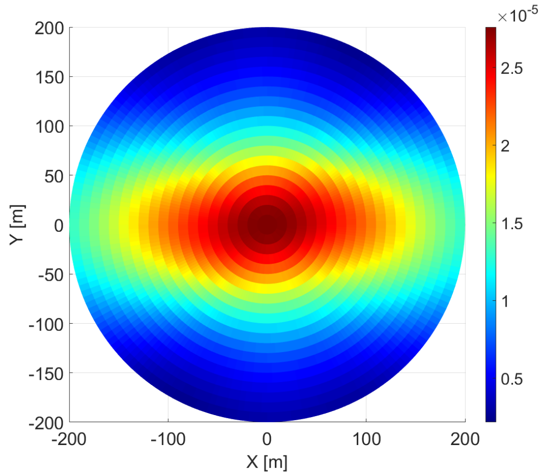

(b) Voltages with dipole on Y axis, SKALA Y polarization, experiment 2

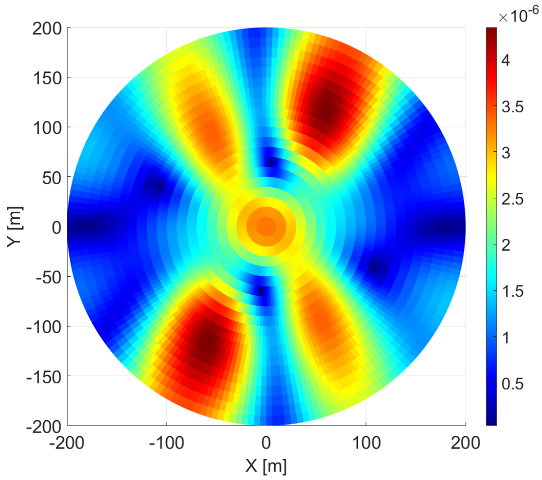

(c) Voltage with dipole on Y axis, SKALA X polarization, 140 MHz excitation, experiment 3

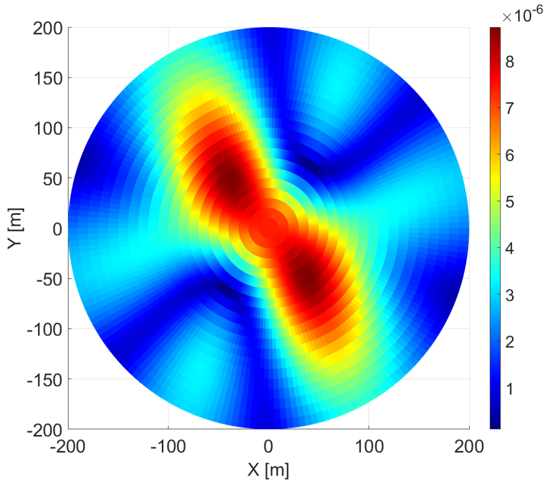

(d) Voltage with dipole on Y axis, SKALA X polarization, 110 MHz excitation, experiment 4

Figure 3.5: Calculation of voltages for a 5 mV dipole excitation, 1 SKALA antenna

Experiments 1 and 2, shown in Fig. 3.5a and 3.5b respectively, resulted in a higher variation of the voltage as the drone moves along the X and Y axis respectively, which is in line with expectations as the values of the radiation pattern of a dipole drop sharply as one moves closer to its axis of orientation.

Experiment 3, carried out in cross polarisation, led to a very different result from experiments 1 and 2. Firstly, the distribution of the voltage peaks were distributed in an X shape. The order of magnitude of the voltages involved was also lower than with parallel polarisation, simulated in experiment 1 and 2. When switching from 140 MHz to 110 MHz excitation, some voltage peaks tend to migrate towards the origin of the array while others fade away.

Finally, a simulation on the array of 16 antennas was performed. The conditions were similar to the first experiment on a single antenna, except that the voltages of each antenna is summed at each drone position. The results of this experiments are shown in Fig. 3.6.

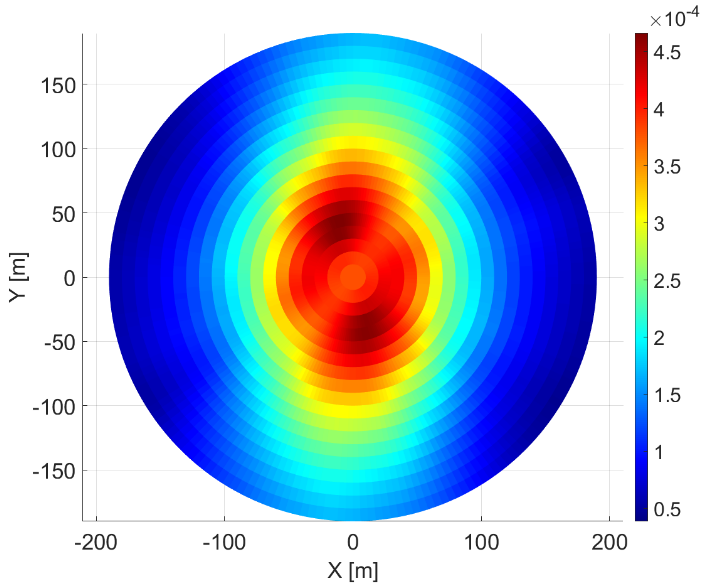

Figure 3.6: Sum of the voltages for an array of 16 antennas, similar configuration to experiment 1

As expected, the order of magnitude of the voltages was larger than in experiment 1, due to the addition of all the 16 voltages for each position and the interaction between each SKALA antennas.

3.3.3 Impact of drone position and attitude error on voltage

Since the position and orientation of the UAV is noised, it is interesting to verify the impact of this noise on the quality of the signals received by the array.

A first re creation of the experiments 1 and 3 was carried out with noise in the position and orientation of the drone. The parameters of this noise are similar to the ones considered in Table 3.1, leading to a bias in the voltage calculation. To characterize the induced voltage noise, the relative error of voltage was calculated from the following equation

$$\varepsilon_V = 10\log_{10}\|V^i_{k,bias} - V^i_k\| - 10\log_{10}\|V^i_k\| \tag{3.10}$$

Where $V^i_{k,bias}$ is the biased voltage, ε_V is then expressed on a dB scale.
The relative errors are shown at Fig. 3.7.

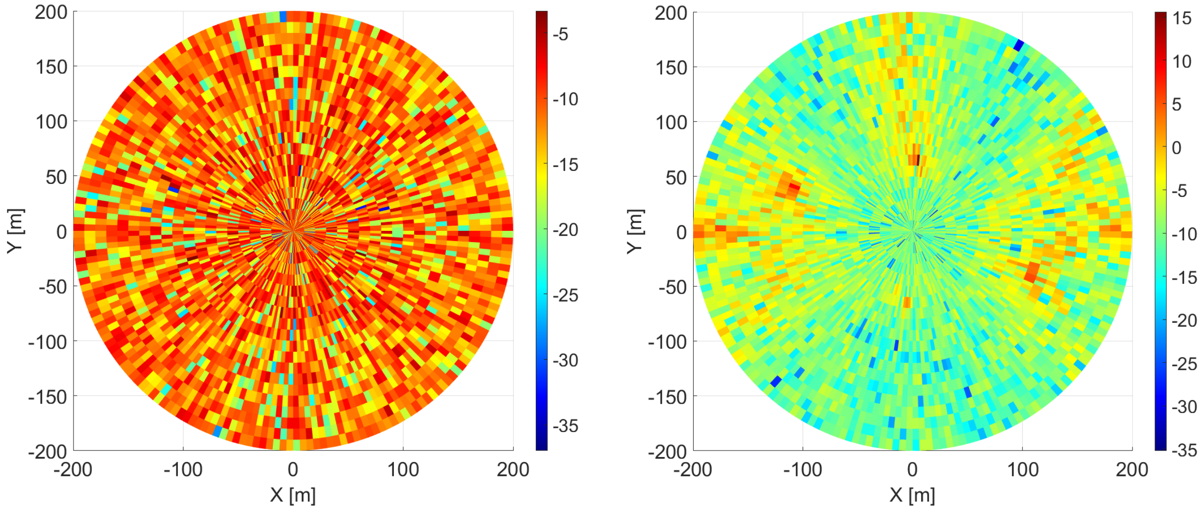

(a) Experiment 1 biased (b) Experiment 3 biased

Figure 3.7: Relative error [dB] due to position and attitude noise on the UAV

While the first experiments led to uniformly distributed values of the errors, the third experiment generated more localized high error values. Furthermore, the maximum error values of experiment 3 were close to 20 dB larger than the experiment 1.

The error for the 16 elements array was also computed using, similarly as before, the same parameters as in experiment 1. The results from this simulation are shown at Fig. 3.8. Lower errors tends to be located along X and Y axes for this configuration.

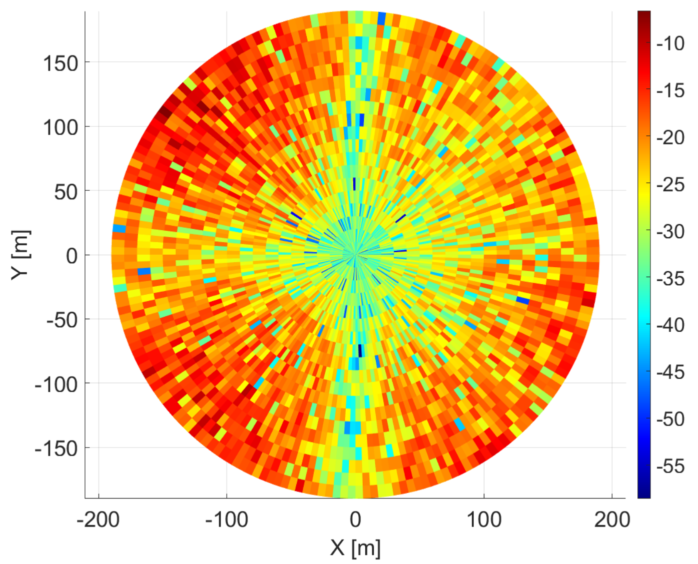

Figure 3.8: Relative voltage error [dB] for the array composed of 256 SKALA antennas

3.3.4 Impact of UAV position and orientation error on calibration coefficients

Even if the error on the voltage might keep high values with noise on the position and attitude of the UAV, it is still interesting to briefly analyse the impact of the number of UAV positions on the calibration error.

In order to investigate the impact of error from those parameters, multiple variations of the simulation using the 16 SKALAs array have been carried out. The simulations covered 3 configurations involving different number of positions of the drone. The relative error of the calibration coefficient was computed and the results are visible in Fig. 3.9.

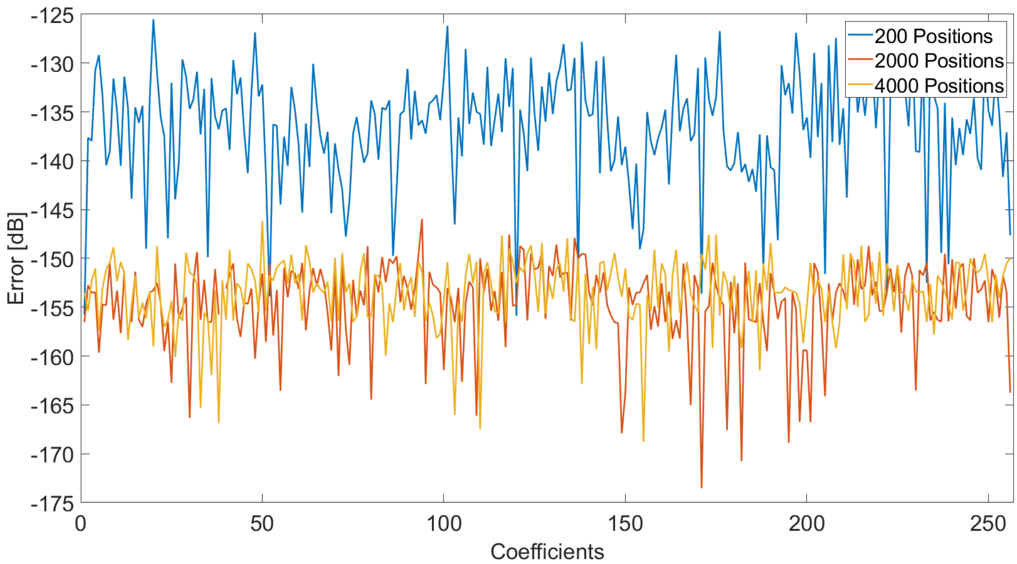

Figure 3.9: Relative error of the calibration coefficients with different numbers of positions, parallel X polarizations

Increasing the number of experiments seems to reduce the error in the calibration coefficients to a certain point. However, since the drone might be limited in terms of battery autonomy and then in terms of experiments during the measurement campaign, increasing the number of drone positions (and then measured voltages) is a difficult way to reduce the relative error. Alternatives consist of using a higher precision in the drone position or attitude. The latter option will be investigated all along those chapters using different methods.

3.4 Conclusion

In this chapter, the implementation of the illumination of a SKALA antenna array by a dipole fixed on a UAV has been studied. Using several arrays containing different SKALA antennas allowed for a progressive increase in computational complexity.

Using a single SKALA antenna allowed quick verification of the implementation of the coupling between the antenna and the UAV. The llumination of the X-polarised SKALA antenna by a dipole placed along the X-axis seems to give a similar result to a Y-polarisation and a dipole along the Y-axis as well, except for a 90° rotation around the vertical axis. Cross-polarisation appears to generate lower voltage around the antenna, potentially resulting in greater sensitivity to noise.

The voltage noise induced by position and attitude noise was analysed using a single SKALA antenna illuminated by the UAV. While the error remained uniform with parallel polarisation, cross-polarisation appeared to result in concentrated error in specific directions. The voltage error using an array composed of 16 antennas showed a less uniform error than using a single SKALA antenna in the same conditions.

Finally, the impact of the number of measurements on the relative error of the array calibration coefficients has been investigated. The error seems to reduce with the number of measurements, as expected. Since the error values barely changed between 2.000 and 4.000 experiments, reducing the calibration error using this method might lead to involve a lot of resources for a low impact on the error.

Chapter 4

Attitude computation

In the previous chapter, the attitude noise was modelled using results of combination of IMU and GPS from [23]. However, developing a method to deduce the attitude of the UAV will help to reduce the said UAV attitude noise.

This chapter is devoted to the calculation of the orientations of the UAV based on the signal received by the SKALA antennas. As the initial goal of this text is to reduce the uncertainty on the calibration coefficients by reducing the error on the angles, it is interesting to check first if these angles are well deductible with supposed known calibration coefficients. Calculating these angles results in finding the solutions of a non-linear problem, it is then necessary to use specific algorithms to solve it.

In a first step, an analysis on a single angle per position will be performed, the Newton-Raphson and Nelder-Mead algorithms are used. We will perform and analyse the error and convergence rate of these algorithms. Then, the problem with three angles per position will be analyzed, the methods of Nelder-Mead and Levenberg-Marquardt will be used to solve the problem. A performance analysis of these algorithms will finally be carried on.

4.1 Single angle calculation per position

In order to find the orientation of the drone with a single angle per position, it is necessary to define the problem correctly. As the measured and simulated voltages are related by the calibration coefficients and assuming that only α is the unknown angle at each UAV positions, it is possible to rewrite the problem in equation (3.6) as

$$\begin{bmatrix} \mathbf{F}^d_{1,1}(\alpha_1) & \dots & \mathbf{F}^d_{1,N_p}(\alpha_{N_p}) \\ & \vdots & \\ \mathbf{F}_{N_a,1}(\alpha_1) & \dots & \mathbf{F}^d_{N_a,N_p}(\alpha_{N_p}) \end{bmatrix} \begin{bmatrix} \mathbf{P}^i_{1,1} & \dots & \mathbf{P}^i_{1,N_a} \\ & \vdots & \\ \mathbf{P}^i_{N_p,1} & \dots & \mathbf{P}^i_{N_p,N_a} \end{bmatrix} \mathbf{c}^i = \tilde{\mathbf{V}}^i \tag{4.1}$$

where we assume that the position of the drone, the angles $\{\beta, \gamma\}$ and the calibration coefficients are perfectly known. Calculating the orientation of the UAV at each position during the flyover is equivalent to solving the following problem

$$\min_{\alpha_p} \|\mathbf{F}^d_{i_a,p}(\alpha_p) \cdot \mathbf{P}^i_{p,i_a} \cdot \mathbf{c}^i - \tilde{V}^i_p\| = \min_{\alpha_p} \epsilon_{p,i} \quad \forall p, i \tag{4.2}$$

where $\epsilon_{p,i}$ contains the absolute value of the error between the voltage from the calibrated antenna i and its measured voltage when the UAV is at position p. Nevertheless, since only one unknown is to be determined, it is possible to use a single antenna to find all the α_p angles, as long as the initial angles are close enough to the solution.

4.1.1 Used algorithms

Newton-Raphson algorithm The Newton-Raphson (N-R) method was implemented in order to solve each attitude individually. At position p, an initial guess of $\alpha_{p,0}$ was based on the non biased orientation of the drone at the same position. At each iteration i, we compute [24]

$$\alpha_{p,i+1} = \alpha_{p,i} - \frac{\epsilon_{\alpha,p}(\alpha_{p,i})}{\epsilon'_{\alpha,p}(\alpha_{p,i})} \tag{4.3}$$

where $\epsilon'_{\alpha,p}(\alpha_{p,i}) = \frac{\mathrm{d}\epsilon_{\alpha,p}(\alpha_{p,i})}{\mathrm{d}\alpha_{p,i}}$.
However, since $\epsilon'_{\alpha,p}$ is difficult to calculate analytically, it is deduced using the secant method [24]:

$$\frac{\mathrm{d}\epsilon_{\alpha,p}(\alpha_{p,i})}{\mathrm{d}\alpha_{p,i}} \approx \frac{\epsilon_{\alpha,p}(\alpha_{p,i}+h) - \epsilon_{\alpha,p}(\alpha_{p,i}-h)}{2h} \tag{4.4}$$

If the error value was less than the termination tolerance, i.e. $\epsilon_{\alpha,p}(\alpha_{p,i}) < \epsilon_{\alpha,tol}$, the algorithm assumed to have converged. However, if $\alpha_{p,i}$ fell precisely on a local minimum, the derivative of the error was null or close to zero, leading to a division by zero while calculating $\alpha_{p,i+1}$. In order to avoid this error, the algorithm considered to have converged at $\alpha_{p,i}$ when $\alpha_{p,i+1} = \pm\infty$.

Nelder-Mead algorithm Since Nelder-Mead (N-M) algorithm was already present in the Matlab function *fminsearch*, no specific implementation of this algorithm was achieved. However, as this method does not calculate the derivative of the error, the convergence method might not be impacted by null values of the derivative.
Two termination tolerances were used in this algorithm, the step tolerance α_{tol} and tolerance on the error step ϵ_{tol} . The algorithm stopped if *both* criterions were met [25]. In our case, the criterions can be written as

$$\begin{cases} \|\alpha_{p,i} - \alpha_{p,i+1}\| < \alpha_{tol}(1 + \|\alpha_{p,i}\|) \\ \|\epsilon_{\alpha,p}(\alpha_{p,i}) - \epsilon_{\alpha,p}(\alpha_{p,i+1})\| = \epsilon_{tol} \end{cases} . \tag{4.5}$$

where α_{tol} is the relative tolerance of the step $\|\alpha_{p,i} - \alpha_{p,i+1}\|$, and ϵ_{tol} is the tolerance of the voltage error variation at the next iteration.

4.1.2 Results and performance analysis

The simulations involved a single SKALA antenna as well as the UAV dipole placed along the UAV's X axis. The UAV followed a noisy circular path with parameters similar to those described in Table. 3.1.

The drone performed a circular trajectory composed of six circles of radius progressively ranging from 10 to 60 m. On each circle, an experiment was carried out every proportional angle $\pi/100$, leading to the generation of 1200 voltages values. The position $\{X, Y, Z\}$ of the UAV and its rotation angles $\{\beta, \gamma\}$ were assumed to be known along the path. Since α was assumed to be zero along the path, this zero value was used as the starting point for the algorithms calculating $\alpha_{p,0}$ at each position p.

For the Newton-Raphson algorithm, the step size was adjusted to a value of $h = 10^{-11}$ while the stopping criterion is $\epsilon_{\alpha,tol} = 10^{-9}$.
For the Nelder-Mead algorithm, it is interesting to compare the performances using the default tolerances and adjusted ones. Two values of the step tolerance have been used, a first one using the default Matlab value, $\alpha_{tol,init} = 10^{-4}$, that was used as *control method*, and a second one using *adjusted* tolerance $\alpha_{tol,r} = 10^{-13}$. The error tolerance was set to $\epsilon_{tol} = 10^{-9}$ for both Nelder-Mead algorithms.

Analysis of error on angle The relative error on α was calculated using

$$\varepsilon_\alpha = 10\log_{10}\|\alpha_{p,\text{fnd}} - \alpha_{p,\text{init}}\| - 10\log_{10}\|\alpha_{p,\text{init}}\| \tag{4.6}$$

where $\alpha_{p,\text{fnd}}$ is the value of the angle found via the algorithm and $\alpha_{p,\text{init}}$ is the angle used to compute $\tilde{V}_k^p$. This error allowed to compare the errors magnitudes for each method. The results are shown at Fig. 4.1. These simulations were performed using an Intel I7-12700 processor and 32 GB RAM.

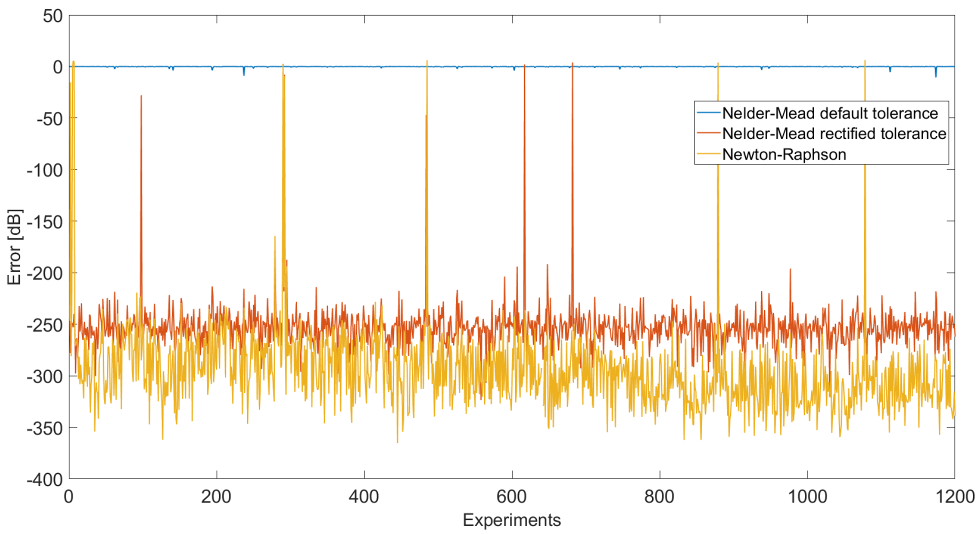

Figure 4.1: Angle error ε_α (dB) using Newton-Raphson and Nelder-Mead algorithms, 1206 experiments

The angle error using the Nelder-Mead algorithm, with default tolerance $\alpha_{tol,init} = 10^{-4}$, was generally much larger than with the modified tolerance $\alpha_{tol,r} = 10^{-9}$.

The errors via adjusted Nelder-Mead and Newton-Raphson oscillate around -250 dB and keep reducing while increasing the circle radius. Although the errors via the two methods are initially relatively similar, the Newton-Raphson method tends to reduce the error, and this phenomenon becomes more pronounced at around 700th position. The average μ_ε and maximum error $\max(\varepsilon)$ values for each method were calculated and can be found in Table 4.1.

One can notice several peaks of error appearing in a regular way throughout the use of the algorithms. These peaks appeared with a more or less regular interval about every 200 position, which corresponds to a half circuit for each circles. These peaks are also valid for both Newton-Raphson and Nelder-Mead adjusted methods. Several simulations have been done and have confirmed their almost systematic and regular appearance, which would suggest an UAV-SKALA configuration giving unstable errors in those directions. This phenomenon explains the positive value of the maximum relative error $\max(\varepsilon)$ for both algorithm in Table 4.1, while maintaining a low mean error μ_ε.

	Newton-Raphson	Nelder-Mead default	Nelder-Mead adjusted
μ_ε [dB]	-295	-0.146	-252
$\max(\varepsilon)$ [dB]	6.24	3.93	0.131

Table 4.1: Mean and max errors for the 3 used method

Time computation analysis Although the Newton-Raphson and Nelder-Mead methods generates relatively similar error values, it is interesting to check how fast each algorithm converges to a solution. The computation time for each position has been extracted and is visible in Fig. 4.2.

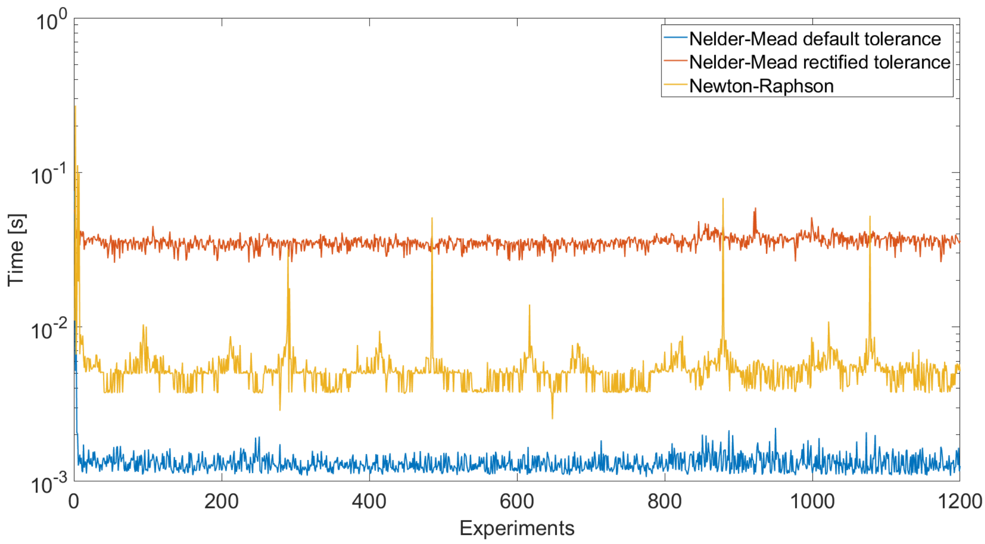

Figure 4.2: Computation time per position for Nelder-Mead and Newton-Raphson methods

As the Nelder-Mead algorithm used as a control has a less strict tolerance than the other ones, the computation time was reduced. Nevertheless, the computation time via the Newton-Raphson algorithm required an order of magnitude less computation time than the adjusted Nelder-Mead algorithm. Several spikes in the Newton-Raphson method can be observed, corresponding to the angle error spikes from Fig. 4.1. These results showed that Newton-Raphson was more efficient to solve the current problem.

4.2 Multiple angles calculation per position

Since the antenna array consists of more than 3 antennas, it is possible to find the orientation of the drone based on the voltages measured in the array. The minimization problem in equation 4.2 becomes

$$\min_{\alpha_p,\beta_p,\gamma_p} \| \sum_{i_a=1}^{N_a} \mathbf{F}^d_{i_a,p}(\alpha_p, \beta_p, \gamma_p) \cdot \mathbf{P}^i_{p,i_a} c^i_{i_a} - \tilde{V}^i_p \| = \min_{\alpha_p,\beta_p,\gamma_p}(\epsilon_{p,i}) \quad \forall p, i \tag{4.7}$$

where we still assume that the calibration coefficients $c^i_{i_a}$ and the drone positions are known.

4.2.1 Used algorithms

Two algorithms were used to solve the problem. Initially, the Nelder-Mead algorithm was used. However, this algorithm only works on scalar-valued functions, requiring to minimize the sum of the errors. The method then minimizes

$$\min_{\alpha_p,\beta_p,\gamma_p} \left(\sum_{i=1}^{N_a} \sum_{p=1}^{N_p} \epsilon_{p,i}(\alpha_p, \beta_p, \gamma_p) \right) \tag{4.8}$$

The Levenberg-Marquardt (L-M) algorithm is generally used to solve systems of non-linear equations. This method was also implemented natively in Matlab with the *fsolve* function and was used in this way in our case. However, even if this method uses the same criterion as Nelder-Mead, the algorithm stops if at least one criteria is met [26].

4.2.2 Error of pose estimation and performance analysis

In order to compare the efficiency of those three methods, a simulation of the drone flyby has been carried on. Since 3 unknowns per position had to be solved, fewer positions were implemented to reduce the simulation time. The drone then still flew at 100m high, but this time, 50 positions were implemented. The UAV therefore travels in 5 circles of radius ranging form 10 to 50 meters, one experiment is carried out every $\pi/5$ radians for each circle. This configuration then generated 50 experiments for one flyby, giving 150 unknowns. The number of SKALA antennas composing the array was set to $N_a = 4$, in order to reduce the computation time.

The same tolerances were used for each algorithm in order to compare each error on the angles found, $\epsilon_{tol} = 10^{-30}$ and $\phi_{tol} = 10^{-100}$. The orientation error for each angle $\{\alpha_p, \beta_p, \gamma_p\}$ was computed as follows

$$\varepsilon_{\phi,p} = \|\phi_p - \phi_{p,mes}\| \tag{4.9}$$

with ϕ_p the angle deduced by the algorithm at position p, $\phi_{p,mes}$ the correct angle defining the orientation of the drone at position p. The simulations were performed on an Intel i7-12700 and 32 GB RAM. However, the Nelder-Mead didn't converge and was stopped after 7110 seconds. The error results of the simulations are shown in Fig. 4.3, 4.4 and 4.5. The initial errors, considering the non biased attitudes, are shown in dashed lines for each angles.

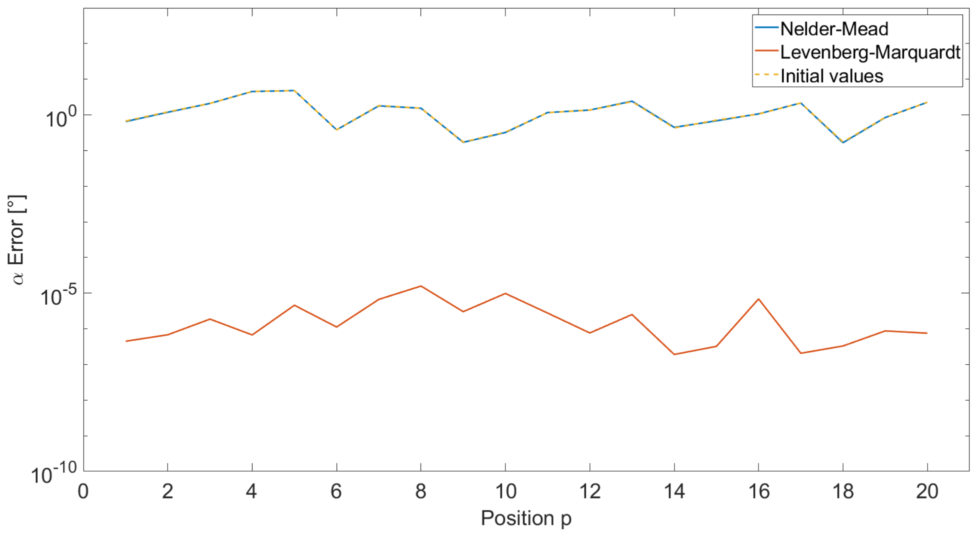

Figure 4.3: α error (degrees) calculation from voltages

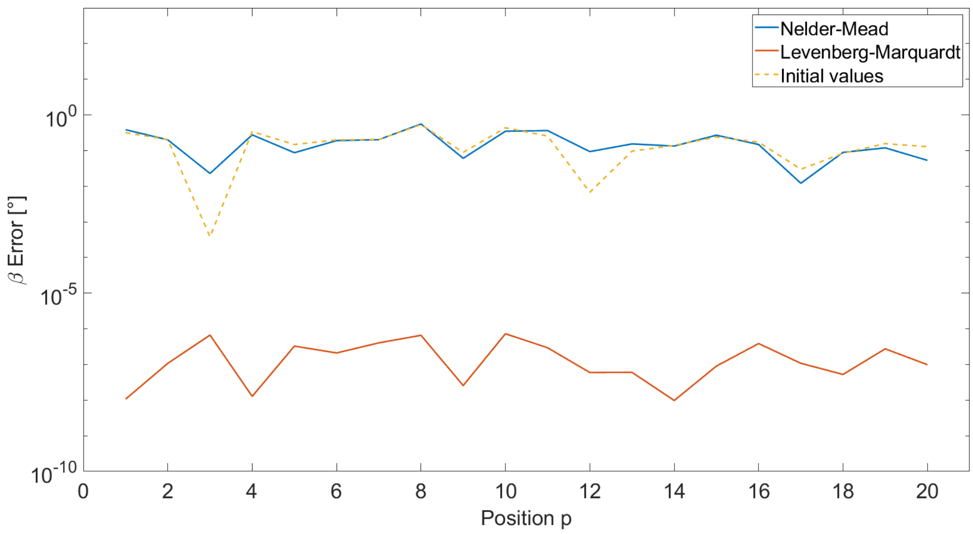

Figure 4.4: β error (degrees) calculation from voltages

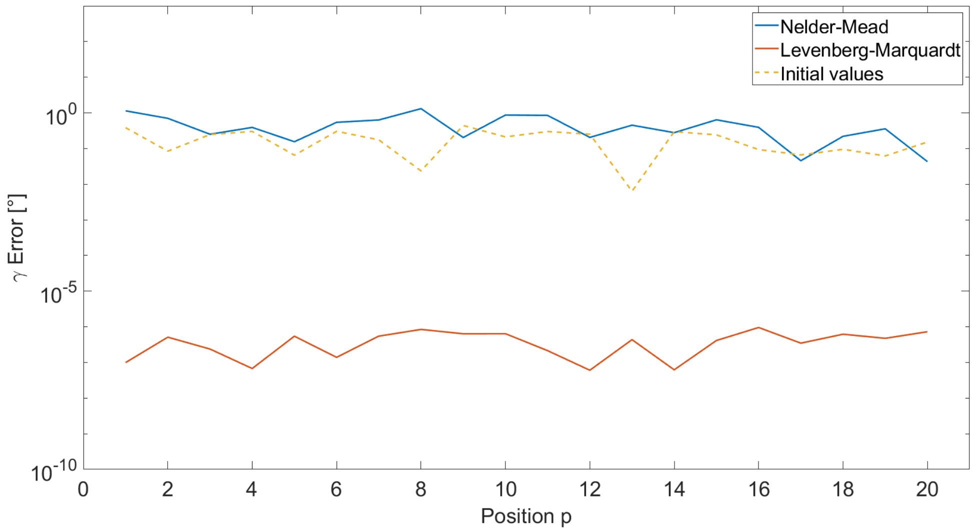

Figure 4.5: γ error (degrees) calculation from voltages

The Nelder-Mead algorithm showed similar errors in the α angle than the initial values, leading to no significant increase of the accuracy for this angle. The error using the Levenberg-Marduardt algorithms showed multiple order of magnitude error differences with the initial values. The error then oscillates between 10^{-5} and 10^{-7} degrees.

For both angles β and γ, the Nelder-Mead algorithm (eq. 4.8) showed way higher errors than the Levenberg-Marquardt algorithm and initial angles. The error of γ angle using th Nelder-Mead algorithm led to suppose that it tends to increase the initial error of UAV attitude, in particular for the γ angle. The Levenberg-Marquardt algorithm (eq. 4.7) shows a lower order of error for all the angles compared to the Nelder-Mead method. The average and maximum values of those errors have been calculated and are shown in Table 4.2. The Levenberg-Marquardt algorithm seemed to calculate the attitude with a higher accuracy and a more stable maximum error than Nelder-Mead. Using an array composed of more than 4 antennas might have even more reduced the angles error since more voltages could be simulated. However, this configuration would have required more computation time.

	α		β		γ	
	$\mu_{\varepsilon,\alpha}$ [°]	$\max(\varepsilon_\alpha)$ [°]	$\mu_{\varepsilon,\beta}$ [°]	$\max(\varepsilon_\beta)$ [°]	$\mu_{\varepsilon,\gamma}$ [°]	$\max(\varepsilon_\gamma)$ [°]
Initial values	1.50	4.80	0.189	0.533	0.190	0.441
Nelder-Mead	1.50	4.80	0.188	0.556	0.484	1.31
L-M	3.01e−6	1.59e−5	2.29e−7	7.3e−7	4.29e−7	9.6e−7

Table 4.2: Mean and maximum error on each angles for different algorithms

As the number of equations increases with the number of MBF considered by the algorithms, it is interesting to check the rate of convergence and the computation time to achieve this convergence. To do so, the computation time, the number of iterations and the sum of the residual errors were extracted at the end of the computations for each algorithm. Those results are shown in Table 4.3

	Iterations	computation time [s]	$\sum \epsilon_{\phi,p}$
Nelder-Mead	2400	7110	9.63e−8
Levenberg-Marquardt	15	264	2.01e−26

Table 4.3: Calculation characteristics for each method used

As expected from Table 4.2, the Levenberg-Marquardt with summed macro MBF showed a higher performance to solve the non-linear equations. The method required fewer resources while providing a more accurate calculation of the drone's orientation.

4.3 Conclusion

In this chapter, an analysis of different algorithms was described in order to resolve the orientation of the drone.

In a first case, only one angle per position was calculated using the voltage received by one SKALA antenna. Each other variables, such as position and other angles defining the attitude of the UAV, were supposed to be known. The Newton-Raphson algorithm showed higher performance to solve the problem than the Nelder-Mead algorithm. The Newton-Raphson indeed showed lower mean error while solving the equations faster than the Nelder-Mead method using similar tolerances. However, error spikes appearing regularly indicated error instabilities in specific directions. Those error spikes appeared for both Newton-Raphson and Nelder-Mead with tight tolerances algorithms.

Calculating the complete attitude of the UAV for each position was made using two algorithms. Nelder-Mead was used to reduce the sum of all the voltages error while Levenberg-Marquardt was used to reduce the error on voltages at each UAV position. The Levenberg-Marquardt algorithm showed higher performances than Nelder-Mead. It indeed required less computation time and iterations while reducing the error by multiple orders of magnitude. The efficiency of this method and its versatility make it a method of choice for solving the problem involving the improvement of calibration coefficients by deducing the UAV attitudes.

Chapter 5

Computation of attitudes and calibration coefficients

The purpose of this chapter is to verify the feasibility of improving the calibration coefficients by performing an estimation of the UAV attitudes. First, we will discuss the computational methods used to solve this problem. Then we will devote a section to the rectification of the calibration by calculating a single angle and quantifying the performance of the methods. Finally, we will discuss on the complete computation of the UAV attitude and about the impact of the estimation of those attitudes regarding the calibration coefficients.

5.1 Problem formulation and algorithms used

5.1.1 Problem formulation

Now that the calibration coefficients must be calculated at the same time as the angles, the minimization problem from eq. (4.7) becomes

$$\min_{\alpha_p,\beta_p,\gamma_p,\mathbf{c}^i_{i_a}} \| \sum_{i_a=1}^{N_a} \mathbf{F}^d_{i_a,p}(\alpha_p,\beta_p,\gamma_p)\cdot \mathbf{P}^i_{p,i_a} c^i_{i_a} - \tilde{V}^i_p \| = \min_{\alpha_p,\beta_p,\gamma_p,\mathbf{c}^i} \epsilon_{p,i} \quad \forall p, i \tag{5.1}$$

leading to $3N_p + N_a^2$ unknowns.
In order to solve this problem, the minimum number of drone positions required can be obtained. Considering that each position p gives $N_a N_p$ voltages, the minimum number of positions required to solve the system of equations is then

$$N_a N_p > 3N_p + N_a^2 \tag{5.2}$$

isolating the number of positions N_p gives

$$N_p > \frac{N_a^2}{N_a - 3} \tag{5.3}$$

This equation is valid if only one calibration coefficient per antenna is calculated. If N_m MBF per antenna are considered, the number of positions for the drone becomes

$$N_p > \frac{N_a^2 N_m}{N_a - 3} \tag{5.4}$$

However, in this chapter, only one calibration coefficient N_m per macro MBF is considered. It is important to note that a network of 3 or fewer antennas will not be enough to solve the problem. However, in the case of a 4-antenna array, only 16 positions seem to be sufficient to find the unknowns. This configuration is likely to lead to large errors as the calibration coefficients are linked to fewer data.

Algorithms used The algorithms used are similar to those previously analyzed in the previous chapter. Since the number of variables has increased compared to the previous chapter, it suggests an increase in computation time by the said algorithm. The tolerance values (eq. 4.5) were kept at $\epsilon_{tol} = 10^{-30}$ and $\alpha_{tol} = 10^{-100}$.
Given that this time the algorithms take the coefficients into account, and that these are calculated using the least squares method, each iteration is carried out in several steps. The steps in the method are described below:

1. Simulation of the measured voltages using correct attitudes
2. Simulation of the voltages with the initial or new attitudes
3. Coefficients calculation using least square method in eq (2.8)
4. New error voltages calculation using eq (5.1)

   If converged, go to step 6, if not, go to step 5
5. Calculation of new angles using Nelder-Mead or Levenberg-Marquardt

   If converged, go to step 6, if not, go to step 2
6. Final voltages simulations from deduced attitudes
7. Final coefficients calculation using simulated final voltages, similarly as step 3.

A diagram of the method is shown in the appendix in Fig. A.

5.2 Simulation results and performance analysis

5.2.1 Single angle per position

Since the vertical rotation of the UAV was considered as the attitude parameter with the higher mean error, reducing the α error was supposed to have a higher impact on the voltages than β and γ angles. Several simulations were conducted to compare the effectiveness of each algorithms. The array consists of 4 SKALA antennas. First, the drone made a series of five circles with radius progressively increasing from 10 m to 50 m. On each circle, 10 voltages dedicated to simulating the measurement were simulated, generating a total of 50 voltage values per antenna. A schematic of the UAV path and the antennas positions is shown in the appendix, in Fig. B. No noise has been added to the UAV's positions, giving noisy values due solely to the drone attitude at each position. The β_p and γ_p were however supposed to be perfectly known at each position p. The dipole on the UAV was excited by a 140 MHz, 5 mV amplitude voltage. The Nelder-Mead method was manually stopped after 6998 iterations due to the computation time.

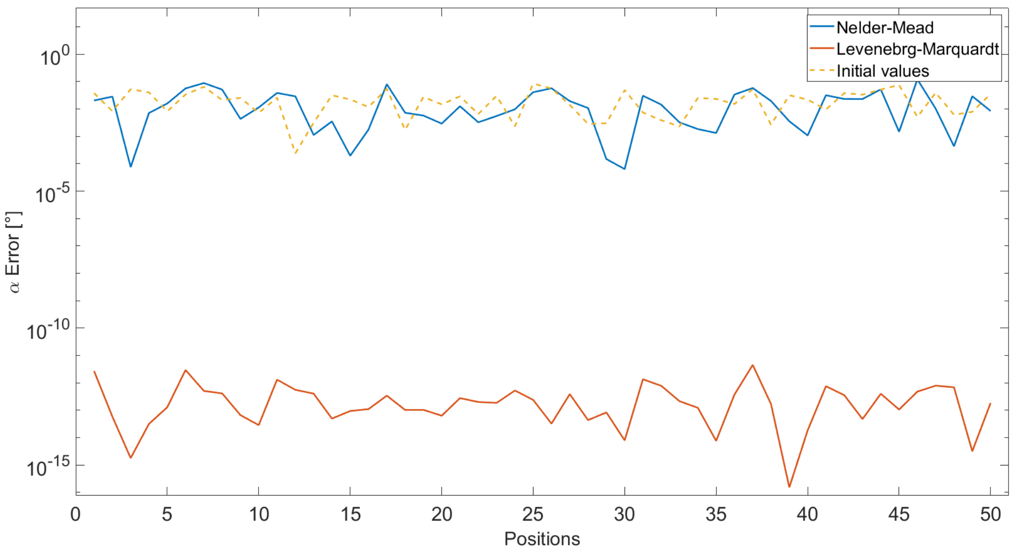

Figure 5.1: α error(degrees) whith one angle unknown while computing calibration coefficients

The deduced angle error with respect to the correct angle was calculated at each position. The relative error of the calibration coefficients $\mathbf{c}^i$ for each antenna was also obtained. These results are shown in Fig. 5.1 and Fig. 5.2. The initial values are show in dashed lines in both figures.

For a lower computational effort, the Levenberg-Marquardt algorithm led to a lower error in terms of attitude calculation. The error indeed oscillated between 5×10^{-5} and 10^{-2} degrees approximately while using Levenberg-Marquardt. The Nelder-Mead algorithm didn't seem to significantly change the error behavior compared to the error while considering α without noise.

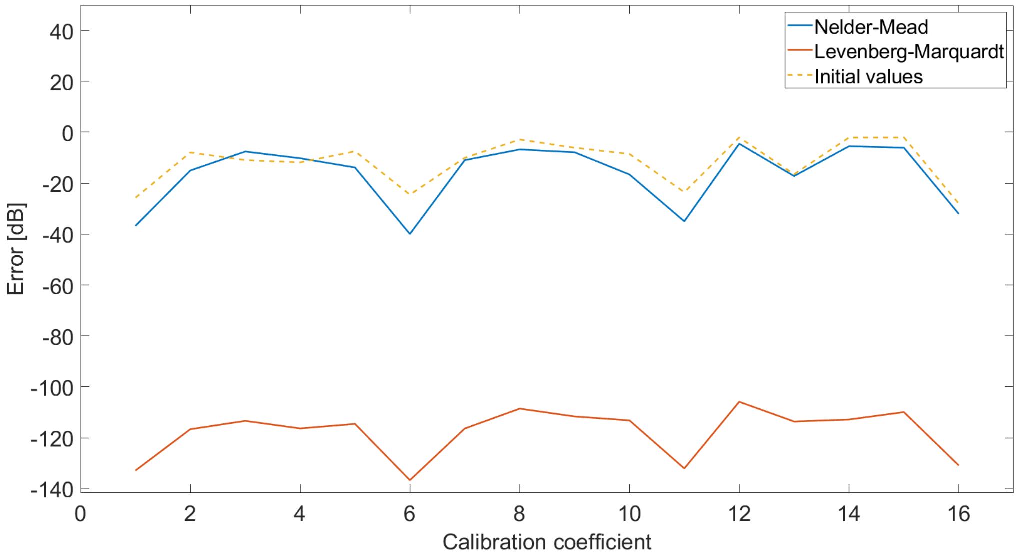

Figure 5.2: Absolute error [dB] of calibration coefficients, one unknown angle per position

Using the Levenberg-Marquardt algorithm led to much lower errors in the calibration coefficients, close to numerical error. The Nelder-Mead approach showed a lower error compared to the initial values, indicating that the calculation of the angles was still effective. Multiple drops of the relative error were observed for the ith coefficient of antenna i, corresponding in Fig. 5.2 to the coefficients 1, 5, 11 and 16 respectively. The error pattern appeared in similar simulations, for both algorithms and the initial values, leading to suppose a lower impact of the α error on those specific coefficients. A similar behavior was observed for the array composed of 16 antennas, leading to suppose the independence of this behavior on the number of antennas. Given c_i^i corresponds to the macro MBF used on the antenna i, this macro MBF is the one with the greatest impact on the EEP model of antenna i. The calibration error is therefore smaller on the dominant macro MBF of each EEP.

5.2.2 Multiple angles per position

Several simulations were carried out to compare the errors obtained for the different methods used. The problem of the previous subsection was extended to a problem including 3 angles per position for the UAV. The trajectory remained unchanged, calculating 50 positions, and the UAV orientation noise follows the values defined previously in Table 3.1. The 3-angles calculation allows the full orientation of the UAV to be recovered as well as the rectification of a calibration coefficient for each macro MBF. The angle errors at each position p and for the three different algorithms are shown in Figs. 5.3, 5.4 and 5.5.

As seen in the previous sections, the orientation errors of the UAV are more accurately calculated by using Levenberg-Marquardt. This behavior was then also expected with the 3 angles per position problem.
The LM algorithm showed an error similar to the initial conditions, oscilliating between 10^{-2} and 5 degrees for the α angles. The β and γ angles were however deduced with a

higher precision than the other angles.
The Levenberg-Marquardt algorithm showed better performances for all the angles, which, as explained before, was an expected result. The α angles were deduced with less accuracy than β and γ angles. The higher error on the α angles compared to β and γ for both algorithms was supposed to be induced by a higher initial error.

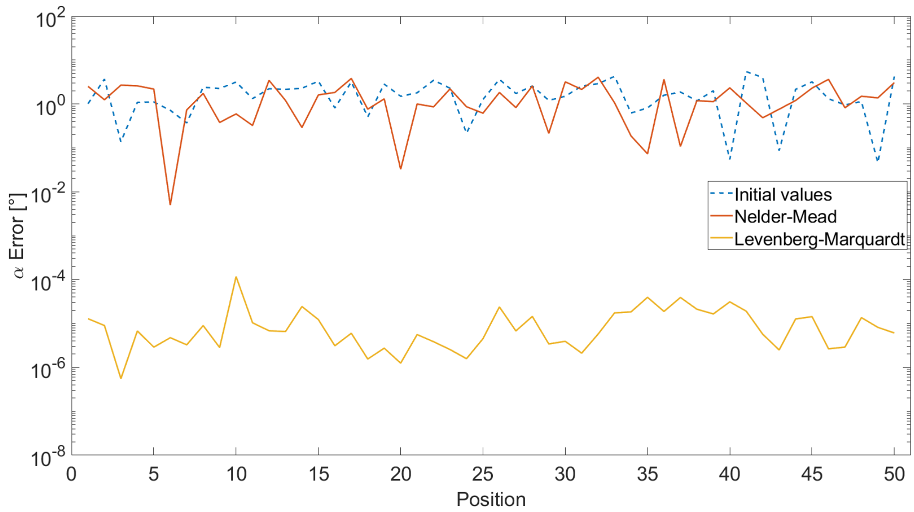

Figure 5.3: α error (degrees) while rectifying the calibration coefficients

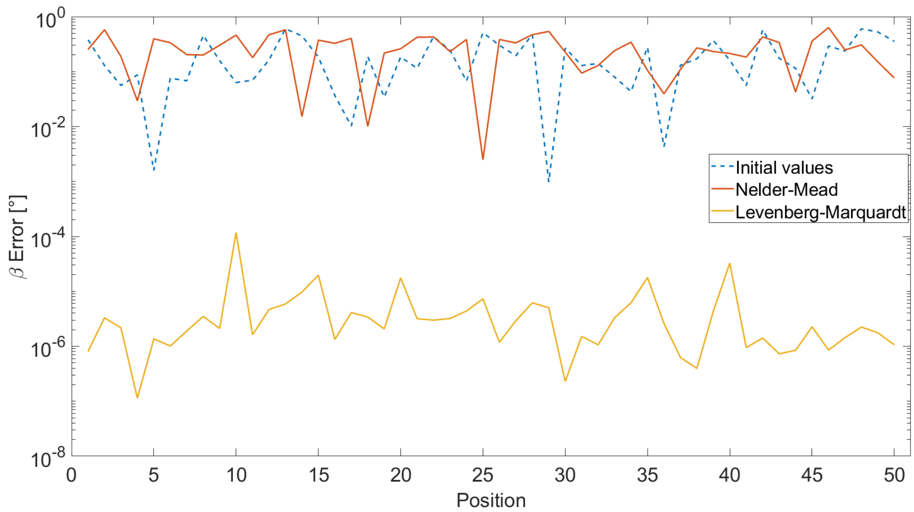

Figure 5.4: β error (degrees) while rectifying the calibration coefficients

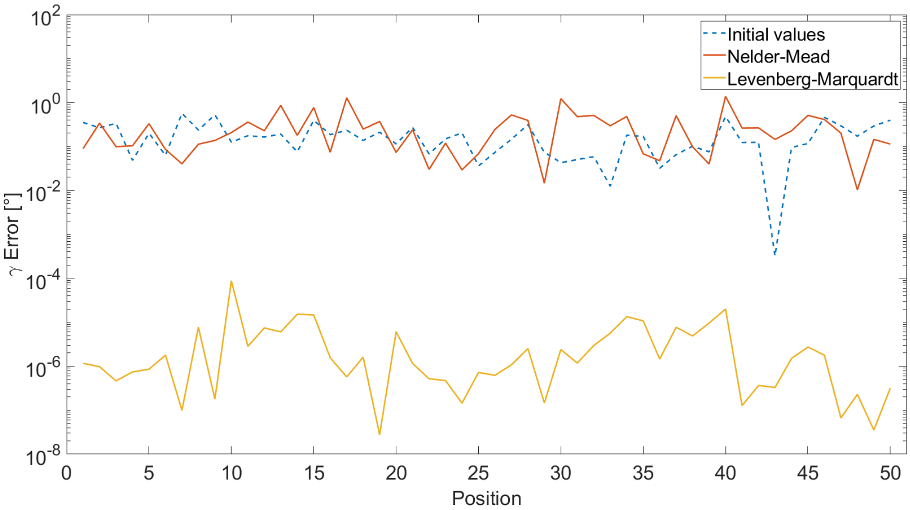

Figure 5.5: γ error (degrees) while rectifying the calibration coefficients

The mean errors of angles were also computed, the results are shown in Table 5.1

Angles	$\mu_{\varepsilon,\alpha}$ [deg]	$\mu_{\varepsilon,\beta}$ [deg]	$\mu_{\varepsilon,\gamma}$ [deg]	$\mu_{\varepsilon,coeff}$ [dB]
Initial	1.92	0.209	0.186	-10.8
Nelder-Mead	1.51	0.275	0.302	-12.2
Levenberg-Marquardt	$1.22\ 10^{-5}$	$6.49\ 10^{-6}$	$5.08\ 10^{-6}$	-65.7

Table 5.1: Mean error comparison for the 3 angles, while rectifying the calibration coefficients.

The absolute error of the calibration coefficient was also calculated and compared to the initial situation without attitudes estimations. The results from those simulations are shown in Fig. 5.6. As expected from the angles calculation, the Nelder-Mead and initial values showed similar errors. The Levenberg-Marquardt algorithm showed again higher performances. This result can be explained by the fact that the angles deduced were more precise. The error gap between initial conditions and the Levenberg-Marquardt algorithm is close to 60 dB. A similar error pattern as previous section appears, even if it tends to be less important with the Levenberg-Marquardt algorithm.

Using the Levenberg-Marquardt algorithm lead to way more accurate results than the other proposed algorithms. The performance of this algorithm therefore makes it a prime candidate for rectifying angles and calibration coefficients.

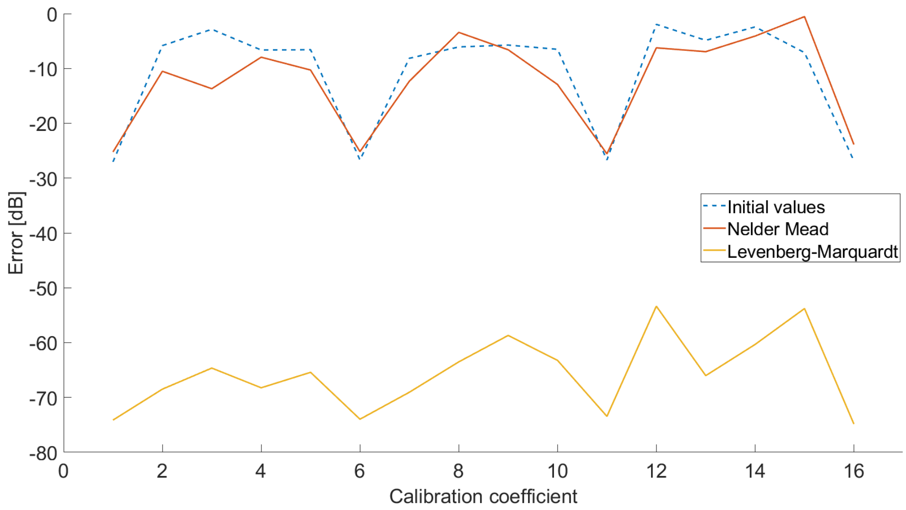

Figure 5.6: Absolute errors [dB] from used algorithms considering 3 angles per position

5.3 Conclusion

In order to improve the calibration coefficients by deducing the attitudes of the UAV at each measurement position, multiple algorithms were developed and tested. As a proof of concept, the developed methods were simulated on an array composed of 4 SKALA antennas. Each optimization problem was mathematically defined, as well as the minimum number of UAV positions to solve each optimization problem correctly.

Simulations were carried out in order to reduce the α rotation error of the UAV and the calibration error. Those simulations showed that Nelder-Mead do not lead to a significant reduction of the error on the angles, not any reduction of the error on the calibration coefficients. However, using Levenberg-Marquardt showed much better results, in terms of α calculation and of calibration accuracy. Patterns appeared in the calibration error, leading to reduce the calibration error associated to the dominant macro MBF of each EEP.

Finally, calculations of the complete attitude information of the UAV at each position and the coupling of this problem with array calibration was carried on using two methods. The Nelder-Mead algorithm showed higher attitude errors than without rectification, leading to generate similar errors than in the non rectified angles. The calibration error was also similar to the case without rectification. However, using Levenberg-Marquardt algorithm showed much better results than the other method. The algorithm allowed us to drastically reduce the error of each UAV attitude and, in turn, to increase the accuracy of the calibration coefficients.

Chapter 6

Impact of thermal noise on coefficients rectification

This chapter is dedicated to the analysis of the impact of thermal noise on the reception quality of the antenna and the angle correction of the UAV during the measurements.

First, the average error voltage induced by the thermal noise of the sky and the Low Noise Amplifier (LNA), used to measure the voltage across the SKALA antennas, will be calculated. Then an analysis of the impact of the noise on the voltage and on the signal to noise ratio (SNR) will be carried on. Afterwards, the impact of this thermal noise on the accuracy of the drone attitudes estimation and the calibration coefficients will be focused on. Finally, the differences between the measurements of real, absolute and imaginary error in the algorithm will be focused on.

6.1 Thermal noise calculation

In the previous sections, noise from the LNA and sky radiation were not taken into account in the calculations. It is nevertheless interesting to take these imperfections into account to verify if these values have an impact on the calculation of the angles and on the rectification of the calibration coefficients.

The AASV0 is equipped with a LNA providing a gain of approximately 40 dB at a temperature of 40 K at 140 MHz [13]. In addition, the sky is supposed to have an impact on the voltage received in the SKALA antenna and is considered as a black body for the further calculations.

Sky noise calculations From the Nyquist theorem, it is possible to compute the power from a resistor temperature, which is equivalent to compute the noise power of an antenna surrounded by a black body at uniform temperature T (Kelvin) [20] :

$$P_{RMS} = k_B T \Delta f \tag{6.1}$$

with k_B the Boltzman constant and Δf the bandwidth of the observation. The observation bandwidth was supposed to be obtained by a perfect band-pass filter, passing frequencies

between $f_{sig} - \Delta f/2$ and $f_{sig} + \Delta f/2$ only, with f_{sig} the excitation frequency of the UAV dipole.
The power across a resistor R can be calculated using $P = V^2/R$, allowing to rewrite the equation as

$$V_{sky}^2 = \frac{k_B R T \Delta f}{2} \tag{6.2}$$

where V_{bias} is the mean voltage received by the illumination of the antenna by the black body surrounding it. Therefore, by supposing this voltage as additive white Gaussian noise, the sky noise temperature can be added to the signal transmitted from the UAV to the SKALA antenna

$$\tilde{V}_{i_a,p,sky} = \tilde{V}_{i_a,p} + \mathcal{N}(0, V_{sky}) \tag{6.3}$$

A sky temperature model allows to calculate the impact of the sky on the voltage received by the SKALA antennas. The sky temperature model for the SKA was already calculated from previous experiments and is approximated as $T_{sky} = 2.73 + 20(408/f_{Mhz})^{2.75}$ (Kelvin) [27].

LNA noise calculations The LNA noise voltage was obtained using the same equations as the sky thermal noise (eq. 6.2). Even if the temperature of the amplifier changed slowly with the frequency between 100 and 350 MHz [13], it was supposed to be constant and equal to 40 K over this bandwidth. The total measured voltage for an antenna i_a illuminated by the UAV at position p then becomes

$$\tilde{V}_{i_a,p,tot} = \tilde{V}_{i_a,p} + \mathcal{N}(0, V_{sky}) + \mathcal{N}(0, V_{LNA}) \tag{6.4}$$

SNR dependence of the central frequency Since the power of the thermal noise is proportional to the bandwidth used, tight bandwidth tends to increase the signal to noise ratio (SNR). Futhermore, the noise thermal power and the signal voltages depends on the frequency of observation, it might exist a measurement frequency maximizing the SNR. Simulations calculating the SNR were made using different frequencies. The drone was supposed to follow the same path as previous chapter, i.e. five circles leading to 50 measurements. The observation bandwidth was supposed to be constant and equal to $\Delta f = 1$ KHz for all the measurements. The excitation voltage was set to 5 mV and the calibration coefficient were supposed unitary. The results of those simulations are shown in Table. 6.1.

Frequency	50 [MHz]	74 [MHz]	140 [MHz]	200 [MHz]	350 [MHz]
SNR $N_a = 4$	$2.56\ 10^{8}$	$9.72\ 10^{9}$	$1.68\ 10^{10}$	$2.69\ 10^{10}$	$1.97\ 10^{10}$
SNR $N_a = 16$	$1.01\ 10^{10}$	$1.87\ 10^{11}$	$1.15\ 10^{11}$	$9.86\ 10^{10}$	$4.22\ 10^{10}$

Table 6.1: SNR calculated for different frequencies supposing a 1 KHz bandwidth.

The maximum SNR for the 4 antennas array was at 200 MHz, with a value of $2.69\ 10^{10}$. However, the 16 antennas array led to a maximum SNR at 74 MHz, with a value of $1.87\ 10^{11}$. The maximum SNR value was expected to be greater for a 16 antennas than 4 antennas array, since the number of antennas increased. This result might indicate that the maximum SNR, and then optimal excitation frequency, might also be different for a 256 antennas array.

6.2 Impact of thermal noise on calibration and angles error

Since thermal noise impacts the measured voltage error, it is interesting to analyse the impact of this thermal noise on the developed method. Several simulations were carried out in order to highlight the impact of SNR on the error of the angles and calibration coefficients found. Still based on 50 positions of the UAV (appendix Fig. B), the observation bandwidth was changed for each simulation, leading to variations of the SNR. Nevertheless, the simulated positions of the UAV remained unchanged between simulations, as did the value of the calibration coefficients calculated by the algorithm. In this way, the drone's initial orientation errors were similar, allowing to generate similar initial conditions for the algorithms. The excitation frequency of the antenna placed on the UAV was simulated at 350 MHz. The 3 angles defining the attitude of the drone and the calibration coefficients were calculated for each simulation. The error of those angles for the different bandwidth are shown at Fig. 6.1, 6.2 and 6.3.

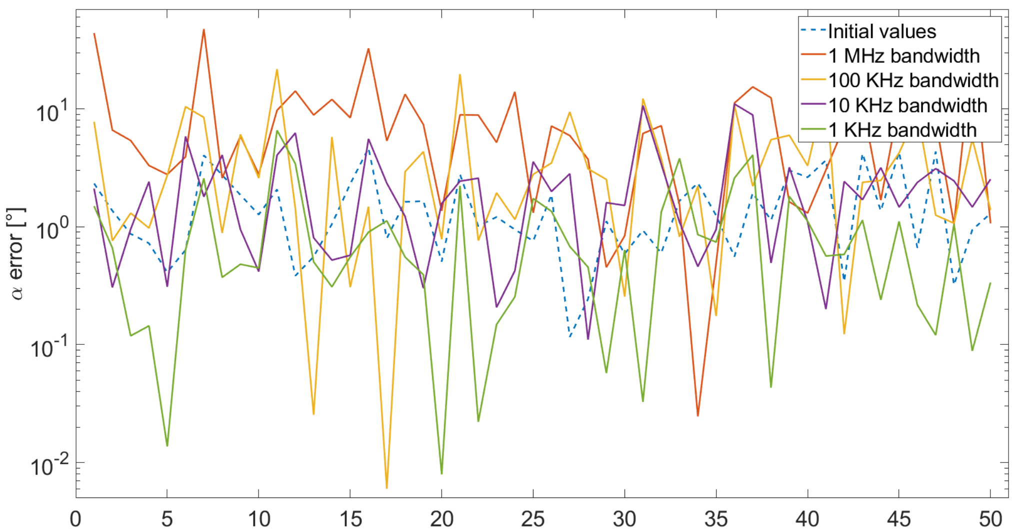

Figure 6.1: α error (degrees) calculated for different bandwidth

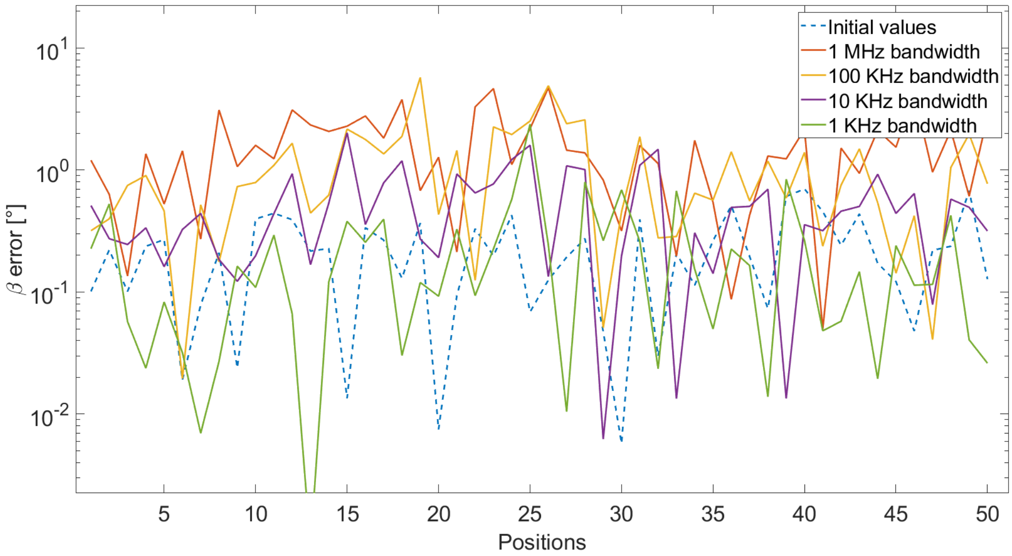

Figure 6.2: β error (degrees) calculated for different bandwidth

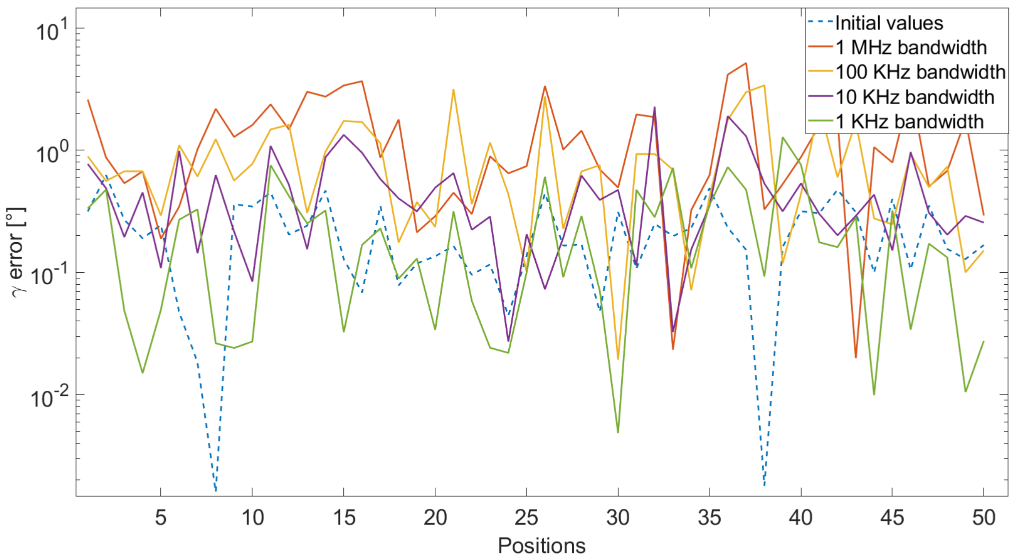

Figure 6.3: γ error (degrees) calculated for different bandwidth

Increasing the bandwidth led to drastically increase the error in terms of the angles deduced, which might have an impact on the calibration performances of the array. Using 300 Hz bandwidth led to lower angle mean error. This result was expected since the SNR reduced with the increase of the band-pass filter bandwidth. However, the α rotation calculation error is higher than the β and γ angle error. This behavior does not depend on the bandwidth used, which let suggest a link with the geometry or the initial error of the UAV attitudes or the mean α error.

Mean error comparisons The mean error was extracted for each bandwidth, those results are shown in Table 6.2. Below 1 KHz bandwidth, each mean angle error is reduced, inducing correct convergence of the algorithm. However, the mean error of the 100 KHz and 1 MHz bandwidth highly increased compared to the non rectified angles, each mean error was approximately multiplied by 7 for the 1 MHz bandwidth. Those results indicate that the algorithm won't be able to reduce the calibration error while using those bandwidth. Using a 1 KHz bandwidth reduced the mean α error but increased the β and γ errors.

	$\mu_{\varepsilon,\alpha}$ [deg]	$\mu_{\varepsilon,\gamma}$ [deg]	$\mu_{\varepsilon,\gamma}$ [deg]	$\mu_{\varepsilon,coeff}$ [dB]
Not Rectified	1.60	0.233	0.220	/
300 Hz	0.634	0.223	0.152	-27.8
1 KHz	1.01	0.251	0.245	-26.3
10 KHz	2.43	0.543	0.498	-19.2
100 KHz	4.31	1.14	0.922	-14.9
1MHz	8.80	1.60	1.38	-11.3

Table 6.2: Comparison of mean errors for different bandwidth used

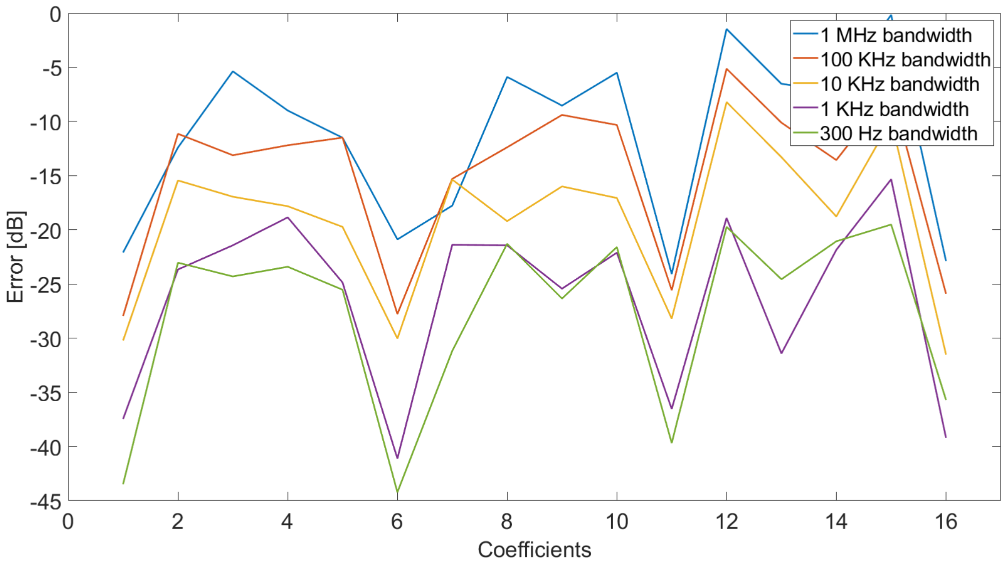

Figure 6.4: Absolute calibration error [dB] for different bandwidth

The larger bandwidth analyzed tends to increase the error of the calibration coefficients, as shown in Fig. 6.4. This result is also expected since the angles error increased and the SNR was reduced. The mean values of the calibration errors are shown in Table 6.2. Once again, the 300Hz bandwidth showed higher performances in terms of reduction of the error.

To quantify the effectiveness of the method, the error improvement for each bandwidth was calculated by subtracting the initial error to the error obtained after using algorithm. The results of those calculations are shown in Fig. 6.5.

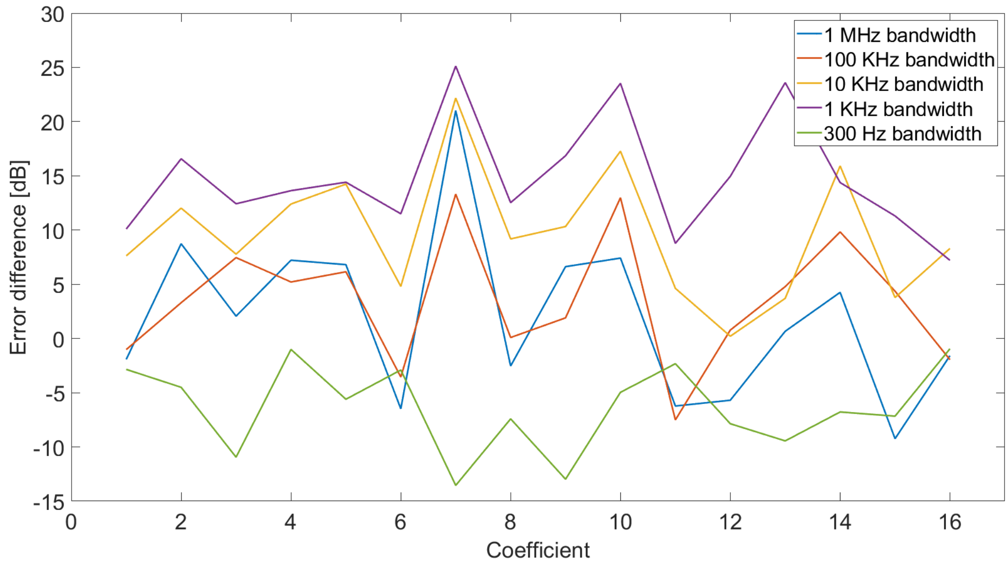

Figure 6.5: Error improvement for each bandwidth [dB]

Only the method applied on the 300 Hz bandwidth showed significant reduction of the error. The error indeed was reduced by approximately 10 dB for this simulation. All the other bandwidths showed a reduction of calibration coefficients accuracy, with the 1 MHz bandwidth increasing the error by up to 25 dB. Those results are expected since the attitude errors increased for all the bandwidths excepting the 300 Hz one. Those observations lead to suppose that the algorithm used might reduce the calibration error if the filter bandwidth is narrower than 1 KHz.

As the array was composed of 4 SKALA antennas only, the SNR had a large impact on the estimation of the UAV attitude and then on the calibration improvements. As shown in previous section, an array composed of 16 antennas multiplied the SNR by a factor close to 10. The deduced attitudes and the calibration was then supposed to be more accurate using more antennas.

6.3 Taking into account Real and Imaginary parts of the voltages

Even if the 300 Hz bandwidth led to better results in the calculation of the attitudes and coefficients, different approaches of the used algorithm might change the error of the calibration. Indeed, all the previous simulations using the Leveberg-Marquardt algorithm computed the *absolute value* of the voltage difference (eq. 5.1). However, as the voltages computed are complex values, computing the absolute value of the error doesn't allow to take into account the real and imaginary parts of the voltages individually. By separating the imaginary and real parts, the optimization problem then becomes

$$\begin{cases} \Re[V_{i_a,p}(\alpha_p,\beta_p,\gamma_p)c_{i_a} - \tilde{V}_{i_a,p}] = 0 & \forall p, i_a \\ \Im[V_{i_a,p}(\alpha_p,\beta_p,\gamma_p)c_{i_a} - \tilde{V}_{i_a,p}] = 0 & \forall p, i_a \end{cases} . \tag{6.5}$$

This reformulation of the problem then allows to generate $2N_aN_p$ equations to solve $3N_p + N_a^2$ unknowns.
To compare the effectiveness of the described methods as well as the rectification using 300Hz bandwidth, simulations taking into account the absolute value, real value and both real and imaginary values of the simulations were made. Those results were compared to the coefficient without rectification algorithm. The results of those simulations are shown in Fig. 6.6, the non rectified coefficients are shown in dashed lines.

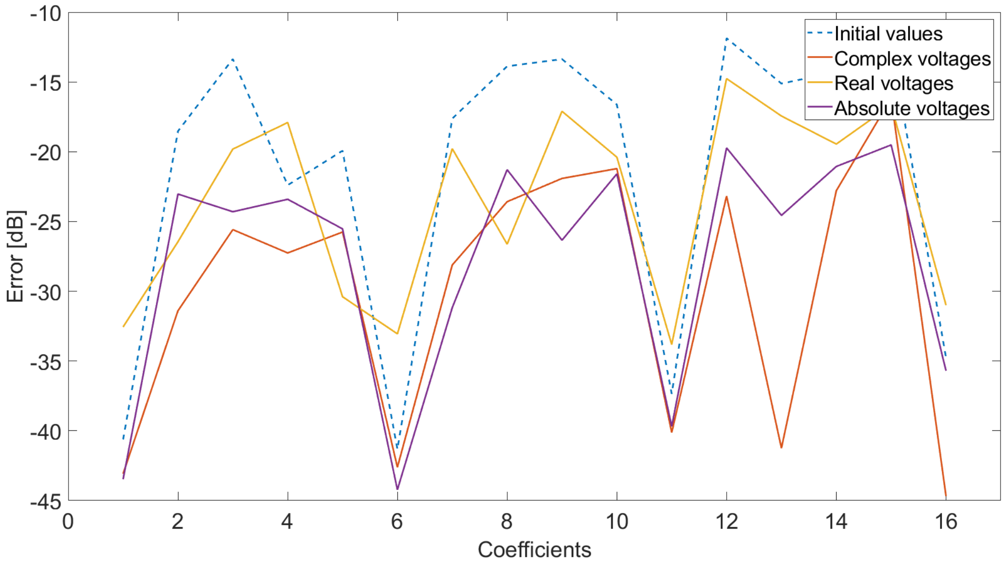

Figure 6.6: Absolute calibration error [dB] considering absolute, real and imaginary parts of the voltages

The algorithm using real voltages values only tends to reduce the higher errors but increasing the lower ones, leading to error oscillations between -35 and -15 dB. This method might then not be suited for the rectification of the calibration coefficients in those conditions. The error indeed increases for the calibration coefficients c_i^i, associated with the macro MBFs that have the higher impact of the antenna radiation pattern, as explained previously. The Levenberg-Marquardt algorithms considering the absolute and complex values of the voltages showed better error performances than using initial values. The error in the calibration coefficients calculation is indeed reduced for each coefficient using each algorithms. The algorithm using the complex values of voltages however showed more stable error values than using complex voltages measurements.

6.4 Conclusion

In this chapter, a brief analysis of the thermal noise and its modelisation was made. The mean error voltage due to the thermal noise of the sky and the LNA was taken into account in the voltage measurements as a Gaussian white noise. The SNR was also calculated for different excitation frequencies with a bandwidth of 1 KHz for an array composed of 4 antennas and the AAVS0 model.

The impact of the thermal noise on calibration and angles rectification was also investigated at 350 MHz frequency with a 5mV UAV voltage excitation. The SNR was adjusted using different bandwidth and the remaining relative error after rectification was compared between each bandwidth. The 300 Hz and 1 KHz bandwidth showed improvements in the precision of the attitudes calculations. However, using more than 10 KHz bandwidth with this method led to induce higher angles error than in the initial case. Those results indicate a minimum SNR required to effectively deduce the UAV attitudes.

Finally, comparing the error with and without rectification with a 300 Hz bandwidth showed improvements in the precision of the calculations. Using the real part of the voltages led to lower performances than using absolute or complex values of the voltages measurements.

As the developed method was applied on an array composed of 4 antennas, the voltage was more impacted than using a 16 antennas array. The SNR was indeed increased with the 16 antennas array, leading to suppose better performances using an array composed of more antennas.

Chapter 7

Conclusion

The calibration of the Square Kilometer Array stations will be a critical step and constitutes a challenge in order to generate high-resolution images [8]. The SKA-Low calibration will then require to develop calibration methods using artificial sources, such as the use of UAVs, to model the interactions between each antennas composing the stations. The far-field calibration using UAV is dominated by attitude errors as explained in [3], which generates bias in the deduction of the calibration coefficients. This work then focused on the deduction of the UAV attitudes using the SKA-Low stations, allowing to increase the accuracy of the calibration.

UAV attitudes estimation The estimation of the UAV attitudes during the flyover was achieved using multiple algorithms. Each algorithm was based on the voltages errors between the simulations and the simulated voltages measurements.

In the case where only one component of the drone's orientation had to be calculated, the Newton-Raphson algorithm produced promising results. The algorithm was able to deduce the component at each position with an error close to -300 dB. These errors also required fewer resources than the Nelder-Mead algorithm. However, error peaks were observed at regular orientations, suggesting configurations generating instabilities in the errors.

The drone's orientation was also accurately deduced on the basis of an array of 4 SKALA antennas. The methods developed enabled us to find the drone's orientation with errors of less than 10^{-5} degrees, for each position, using the Levenberg-Marquardt algorithm. This algorithm converged more quickly than the Nelder-Mead algorithm, making it a method of choice for improving the calibration during the rest of the work.

Calibration improvement by UAV attitudes deduction The Nelder-Mead and Levenberg-Marquardt algorithms were used to develop a method for reducing the error in the calibration coefficients. By recalculating new drone orientation values for each position at each iteration, it was possible to improve the accuracy of the calibration coefficients.

Initially, only one angle per position was evaluated at the same time as improving the calibration error. The Nelder-Mead algorithm did not give significant results in solving this problem, either in solving the orientation or in calibration. However, the Levenberg-Marquardt algorithm showed a significant improvement in the accuracy of the angles and calibration coefficients. A pattern of error in the calibration coefficients was observed independently of the methods used. The coefficients associated with the macro MBFs having the greatest impact on each EEP were systematically subject to a smaller error.

The problem was then extended to the complete calculation of the UAV orientations, which allowed us to verify the feasibility of the method. The Nelder-Mead algorithm showed no significant improvement in the error and even increased the error in estimating the angles of the UAV. The algorithm did, however, reduce the average error of the calibration coefficients by around 2 dB. The Levenberg-Marquardt algorithm showed much better results, with angle errors of around 10^{-5} degrees and an average error in the calibration coefficients of around -65 dB.

Impact of the themal noise on the calibration The impact of thermal noise on the quality of the calibration coefficients calculated was analysed. The thermal noise of the sky and the LNA were modelled and the SNR was calculated for different frequencies and different numbers of antennas. In the case of an array consisting of 4 antennas, the maximum SNR calculated was obtained with an excitation frequency of 200 MHz. In the case of 16 antennas, the maximum SNR was obtained at around 74 MHz. This suggested that the configuration of the array had an impact on the maximum SNR and the associated excitation frequency. It was therefore assumed that the maximum SNR for an array of 256 SKALA antennas would be higher than with 16 antennas and would also be obtained at other frequencies.

The impact of calibration quality was linked to the frequency band used. A narrower bandwidth reduced the error better than a wider bandwidth. An increase in error for all the frequencies larger than 1 KHz was observed, leading to suppose a restriction of the developed method in narrow bands.

Finally, different error calculation were compared in order to deduce the most effective method for the calculation of the coefficients. Considering the real part of the voltage errors led to an increase of the calibration coefficients error associated to the most impacting macro MBF, the method still reduced the error of the other calibration coefficients. The methods considering the absolute and complex values of the errors showed better performances, calculating the calibration coefficients with more accuracy than the previous method. The overall calibration error was indeed reduced.

As the simulation time mainly limited the number of simulated antennas composing the arrays, further researches to accelerate those simulations needs to be carried out. Extending the methods developed to a complete SKA needs also to be done in order to confirm the previously taught hypotheses.

Appendix A

Resolution method diagram

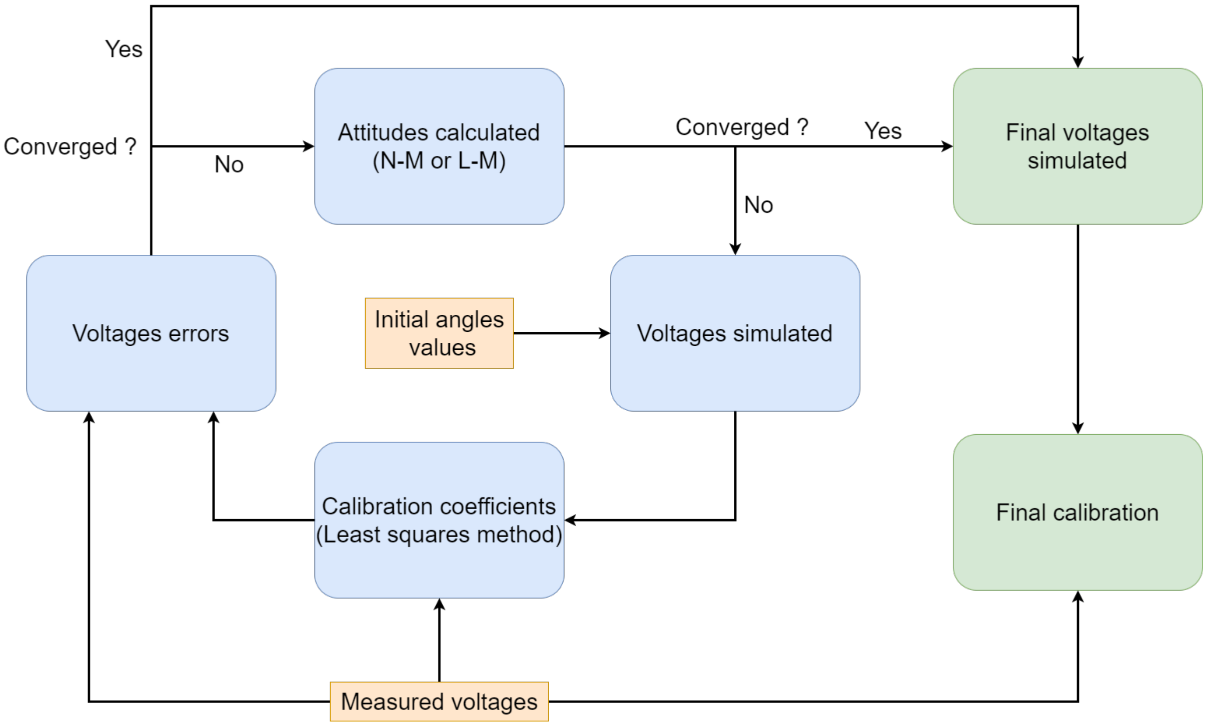

Figure A.1: Diagram of the method used to compute the calibration and drone attitudes

Appendix B

UAV positions

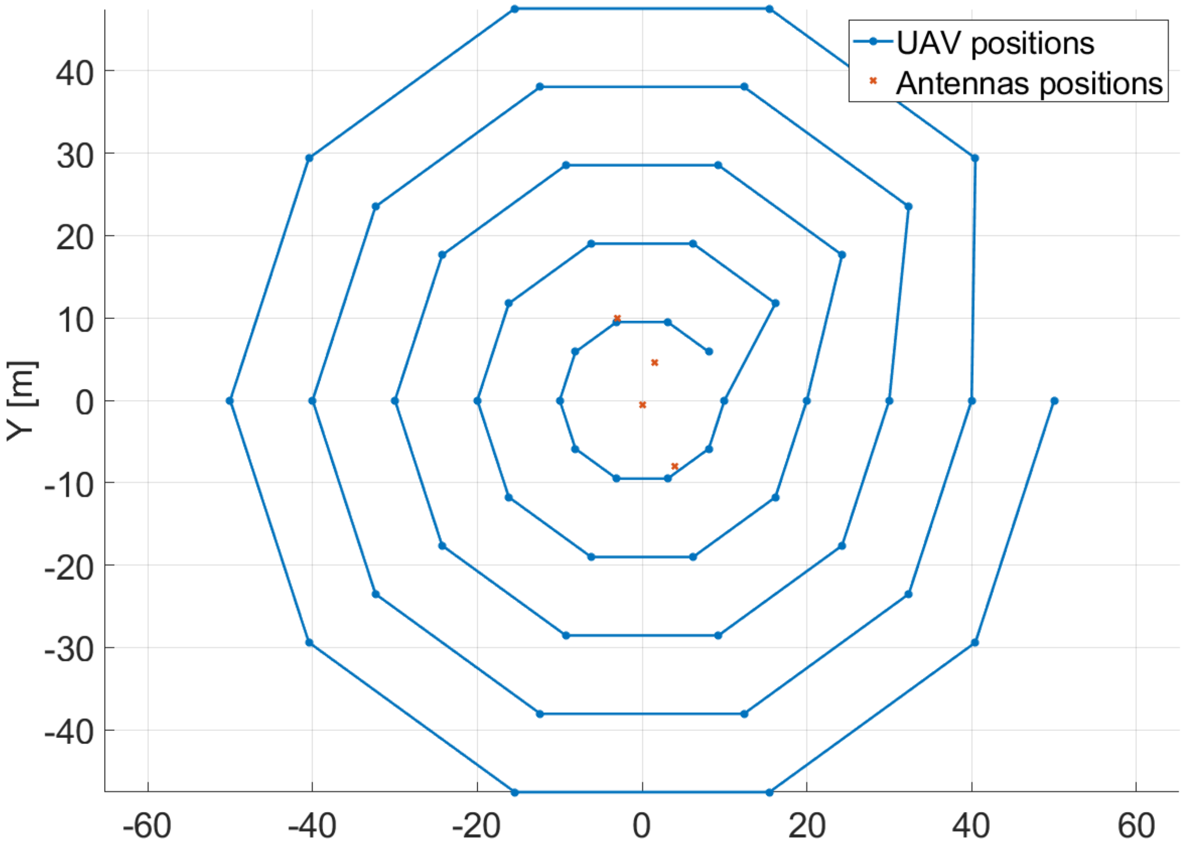

Figure B.1: UAV path and antennas positions for the calibration and attitudes calculations

Bibliography

[1] SKAO, "SKA Phase 1 Executive Summary," 2020. [Online]. Available: https://skao.canto.global/s/MH29C?viewIndex=0 [Accessed on 01-03-2023]

[2] ——, "SKA Phase 1 Construction Proposal," 2022. [Online]. Available: https://skao.canto.global/s/M8159?viewIndex=0column=documentid=bg07p5lsdt2ep2iv9660tpd70 [Accessed on 03-06-2023]

[3] L. V. Hoorebeeck, "Calibration of the SKA-low antenna array using drones," *Ecole Polytechnique de Louvain*, 2018, Master's Thesis. [Online]. Available: https://dial.uclouvain.be/memoire/ucl/fr/object/thesis%3A14813/datastream, [Accessed on 02-11-2022]

[4] SKAO, "SKA-Mid - close up artist impression," 2022. [Online]. Available: https://www.skao.int, [Accessed on 03-06-2023]

[5] ——, "SKA-Low Artist Impression 2022_SKA-Low stations in core," 2022. [Online]. Available: https://www.skao.int, [Accessed on 03-06-2023]

[6] H. Bui-Van, J. A. M. Arts, Q. Gueuning, C. Raucy, D. González-Ovejero, E. de Lera Acedo, and C. Craeye, "Fast and Accurate Simulations Technique for Large Irregular Arrays," *IEEE transactions of antennas and propagation*, vol. 66, ZS2018.

[7] W. C. Gibson, *The method of moments in electromagnetics.* Chapman Hall/CRC, 2008.

[8] S. Wijnholds, S. Tol, R. Nijboer, and A.-J. Veen, "Calibration challenges for the next generation of radio telescopes," *IEEE Signal Processing Magazine*, vol. 27, 01 2010.

[9] I. Labbe, P. Dokkum, E. Nelson, R. Bezanson, K. Suess, J. Leja, G. Brammer, K. Whitaker, E. Mathews, M. Stefanon, and B. Wang, "A population of red candidate massive galaxies 600 myr after the big bang," *Nature*, vol. 616, pp. 1–2, 02 2023.

[10] E. H. Telescope, "Press release (april 10, 2019): Astronomers capture first image of a black hole," https://eventhorizontelescope.org/, [Accessed on 02-03-2023].

[11] A. R. Thompson, J. M. Moran, and G. W. S. Jr, *Interferometry and Synthesis in Radio Astronomy.* Springer Cham, 2017.

[12] E. de Lera Acedo, P. Bolli, F. Paonessa, G. Virone, E. Colin-Beltran, N. Razavi-Ghods, I. Aicardi, A. Lingua, P. Maschio, J. Monari, G. Naldi, M. Piras, and G. Pupillo, "SKA aperture array verification system: electromagnetic modeling and beam pattern measurements using a micro UAV," *Experimental Astronomy*, vol. 45, pp. 1–20, 2018.

[13] P. Benthem, R. Wayth, E. Acedo, K. Adami, M. Alderighi, C. Belli, P. Bolli, T. Booler, J. Borg, J. Broderick, S. Chiarucci, R. Chiello, L. Ciani, G. Comoretto, B. Crosse, D. Davidson, A. Demarco, D. Emrich, A. Es, and A. Williams, "The aperture array verification system 1: System overview and early commissioning results," *Astronomy and astrophysics*, vol. 655, 11 2021.

[14] L. V. Hoorebeeck, J. Cavillot, H. Bui-Van, F. Glineur, C. Craeye, and E. de Lera Acedo, "Near-field calibration of SKA-Low stations using unmanned aerial vehicles," *13th European Conference on Antenna and Propagation*, 2019.

[15] C. Culotta-López, S. Gregson, A. Buchi, C. Rizzo, D. Trifon, S. Skeidsvoll, I. Barbary, and J. Espeland, "On the uncertainty sources of drone-based outdoor far-field antenna measurements," pp. 1–6, 2021. [Online]. Available: https://ieeexplore.ieee.org/document/9620638 [Accessed on 05-05-2023]

[16] C. Craeye, J. Laviada, R. Maaskant, and R. Mittra, "Macro basis function framework for solving maxwell's equations in surface-integral-equation form," *FERMAT Journal*, 2014. [Online]. Available: https://dial.uclouvain.be/pr/boreal/object/boreal:248714, [Accessed on 27-05-2023]

[17] D. Gonzalez-Ovejero and C. Craeye, "Interpolatory macro basis functions analysis of non-periodic arrays," *IEEE Transactions on Antennas and Propagation*, vol. 59, no. 8, pp. 3117–3122, 2011.

[18] Q. Gueuning, C. Craeye, E. Colin-Beltran, and E. de Lera Acedo, "Validation of the harp method for simulation of mutual coupling between skala antennas," in *2015 International Conference on Electromagnetics in Advanced Applications (ICEAA)*, 2015, pp. 1214–1217.

[19] Q. Gueuning, C. Raucy, C. Craeye, E. Colin-Beltran, and E. de Lera Acedo, "Mutual coupling analysis in non-regular arrays of SKALA antennas with the HARP approach," in *2015 IEEE International Symposium on Antennas and Propagation USNC/URSI National Radio Science Meeting*, 2015, pp. 1528–1529.

[20] A.Guissard and C. Craeye, *Antennes et propagation.* Ecole Polytechnique de Louvain, Academic year 2022-2023, notes de cours UCLouvain LELEC2910, course syllabus.

[21] E. de Lera Acedo, N. Razavi-Ghods, N. Troop, N. Drought, , and A. Faulkner, "SKALA, a log-periodic array antenna for the SKAlow instrument: design, simulations, tests and system considerations," *Experimental Astronomy*, vol. 39, pp. 567–594, 2015.

[22] P. Henkel, A. Sperl, U. Mittmann, T. Fritzel, R. Strauss, and H. Steiner, "Precise 6D RTK positioning system for UAV-based near-field antenna measurements," pp. 1–5,

2020. [Online]. Available: https://ieeexplore.ieee.org/document/9620638 [Accessed on 07-05-2023]

[23] K. Fukuda, S. Kawai, and H. Nobuhara, "Attitude estimation by kalman filter based on the integration of IMU and multiple GPSs and its application to connected drones," pp. 1286–1292, 2020. [Online]. Available: https://ieeexplore.ieee.org/abstract/document/9240380 [Accessed on 05-05-2023]

[24] V. Legat, *MATHEMATIQUES ET METHODES NUMERIQUES ...ou les aspects facétieux du calcul sur un ordinateur.* Ecole Polytechnique de Louvain, Academic Year 2022-2023, Notes de cours UCLouvain LEPL1104, course syllabus. [Online]. Available: https://perso.uclouvain.be/vincent.legat/documents/epl1104/epl1104-notes-v8-4.pdf [Accessed on 12-05-2023]

[25] MathWorks, "Optimizing nonlinear functions," https://www.mathworks.com/help /matlab/math/optimizing-nonlinear-functions.html#bsgpq6p-11, [Accessed on 12-05-2023].

[26] ——, "fsolve," https://www.mathworks.com/help/optim/ug/fsolve.html, [Accessed on 12-05-2023].

[27] M. C. et al., *SKA1 SYSTEM BASELINE DESIGN V2.* SKA Organisation, 2017, technical Report SKA-TEL-SKO-0000008. [Online]. Available: https://www.skao.int/sites/default/files/documents/d3-SKA-TEL-SKO-0000008-Rev11_SKA1SystemRequirementSpecification_0.pdf [Accessed on 24-02-23]

UNIVERSITÉ CATHOLIQUE DE LOUVAIN
École polytechnique de Louvain
Rue Archimède, 1 bte L6.11.01, 1348 Louvain-la-Neuve, Belgique | **www.uclouvain.be/epl**